

# Contents

<b>1</b>	<b>Theory</b>	<b>1</b>
1.1	The shallow water equations . . . . .	1
1.2	Numerical discretization . . . . .	2
1.2.1	The finite volume method . . . . .	2
1.2.2	Definition of the discretized flux . . . . .	3
1.2.3	Definition of the discretized source . . . . .	5
1.2.4	Extension to order 2 in space (MUSCL) . . . . .	6
1.2.5	Boundary conditions . . . . .	7
1.2.6	Definition of the discretized time derivative . . . . .	8
1.2.7	Local time stepping . . . . .	9
<b>2</b>	<b>Verification of the code</b>	<b>10</b>
2.1	Straight channel with slope and bottom friction . . . . .	10
2.2	Straight channel with slope, bottom and wall friction . . . . .	13
2.3	Oblique hydraulic jump . . . . .	15
2.4	Supercritical flow in symmetrical contraction . . . . .	18
2.4.1	Bed slope and friction are neglected . . . . .	18
2.4.2	Bed slope and friction are taken into account . . . . .	19
2.4.3	Irregular shock reflection . . . . .	25
2.5	Transcritical flow in long channels . . . . .	25
2.5.1	Theoretical 1D model . . . . .	26
2.5.2	Results . . . . .	27
2.6	Partial breach of a dam . . . . .	29
	<b>Bibliography</b>	<b>36</b>

# Chapter 1

## Theory

### 1.1 The shallow water equations

Free surface flows often appear in ocean, engineering and atmospheric modelling. In many applications involving unsteady water flows where the horizontal length scale is much greater than the vertical length scale, the shallow water equations (SWE) are commonly used to model these flows. These equations have been proposed by Saint-Venant [1] in 1871 to model flows in a channel. The SWE are derived from the three-dimensional Navier-Stokes equations for incompressible flows. A vertical integration is performed on the Navier-Stokes equations to obtain the set of two-dimensional SWE. The following hypotheses were made:

- Small bottom slope
- Hydrostatic distribution of the pressure
- The main motion of particles occurs in horizontal planes
- The vertical distribution of the horizontal velocity components  $u, v$  is nearly uniform
- The mass forces are gravity and the Coriolis force
- The vertical acceleration of the particles is negligible in comparison with the gravitational acceleration  $g$

The two-dimensional SWE are a nonhomogeneous system of nonlinear hyperbolic equations and are expressed as

$$\frac{\partial \mathbf{U}}{\partial t} + \frac{\partial \mathbf{F}(\mathbf{U})}{\partial x} + \frac{\partial \mathbf{G}(\mathbf{U})}{\partial y} = \mathbf{S}, \quad (x, y) \in \Omega, t \geq 0 \quad (1.1)$$

with the variable vector

$$\mathbf{U} = \begin{pmatrix} h \\ hu \\ hv \end{pmatrix} \quad (1.2)$$

where  $h$  is the water height and  $(u, v)$  the horizontal velocity components. These three variables are function of time  $t$  and horizontal space  $(x, y)$ . The flux terms are expressed by

$$\mathbf{F}(\mathbf{U}) = \begin{pmatrix} hu \\ hu^2 + \frac{gh^2}{2} \\ huv \end{pmatrix}, \quad \mathbf{G}(\mathbf{U}) = \begin{pmatrix} hv \\ huv \\ hv^2 + \frac{gh^2}{2} \end{pmatrix} \quad (1.3)$$

and the source term represents the combined effects of geometric slope  $S_0$  and friction slope  $S_f$

$$S = gh(S_0 + S_f) = -gh \begin{pmatrix} 0 \\ \frac{\partial z_b}{\partial x} \\ \frac{\partial z_b}{\partial y} \end{pmatrix} - gh \frac{n^2 \sqrt{u^2 + v^2}}{h^{4/3}} \begin{pmatrix} 0 \\ u \\ v \end{pmatrix} \quad (1.4)$$

Herein  $g$  is the gravitational acceleration,  $z_b(x, y)$  is the smooth topography and  $n[m^{-1/3}s]$  is the Manning coefficient of roughness. The range of values for  $n$  spans from 0.01 (glass) to 0.1 (flood plains reaching branches of trees), see Chow [2] (pages 109-113) for a compiled table of values.

This definition of the friction is common in many shallow water models: only the friction at the bottom of the bed is taken into account. Specifically models that assume vertical channel side-walls and use free-slip boundary conditions do not account for the friction at the walls. Neglecting this effect, open channel flow would likely show a marked variation in water depth from the one measured experimentally. Therefore an extension of the friction term (see Brufau [3]) has also been implemented:

$$ghS_f = -gh\sqrt{u^2 + v^2} \left( \frac{n_b^{3/2}}{h} + \frac{n_w^{3/2}l_w}{\Omega} \right)^{4/3} \begin{pmatrix} 0 \\ u \\ v \end{pmatrix} \quad (1.5)$$

Herein  $n_b$  and  $n_w$  are the Manning friction coefficients relative to the bottom and to the wall respectively.  $l_w$  is the length of the wall along the flow and  $\Omega$  is the wetted area on the bottom near the wall.

The Froude number is defined as the ratio

$$Fr = \frac{\sqrt{u^2 + v^2}}{\sqrt{gh}} \quad (1.6)$$

and is analogous to the Mach number of gas dynamics. The wave speed  $c = \sqrt{gh}$  is the velocity at which a disturbance should travel in the space. When  $Fr < 1$ , the flow is called *subcritical*. In this case, disturbances can travel upstream. On the other hand, when  $Fr > 1$ , the flow is called *supercritical*. In this case, the wave speed is smaller than the flow velocity and the disturbances can not travel upstream anymore.

## 1.2 Numerical discretization

The computational domain  $\Omega$  is discretized into triangles of area  $\Omega_i$  and the SWE are integrated over the whole domain.

### 1.2.1 The finite volume method

We assume here the cell-centered approach of the finite volume method. These cells are the same as the initial grid elements; the values of the dependent variables are averaged over the cell and can be stored in the cell center. The integration of the SWE (1.1) over the domain gives

$$\int_{\Omega} \frac{\partial U}{\partial t} d\Omega + \int_{\Omega} \frac{\partial F(U)}{\partial x} d\Omega + \int_{\Omega} \frac{\partial G(U)}{\partial y} d\Omega = \int_{\Omega} gh(S_0 + S_f) d\Omega \quad (1.7)$$

The computational domain is split into a set of finite volumes  $\Omega_i$  and the divergence theorem is applied to the flux terms, turning the surface integrals into line integrals along the cell border  $\Gamma_i$ :

$$\int_{\Omega_i} \frac{\partial U}{\partial t} d\Omega_i = - \oint_{\Gamma_i} (n_x F(U) + n_y G(U)) d\Gamma_i + \int_{\Omega_i} gh(S_0 + S_f) d\Omega_i \quad (1.8)$$

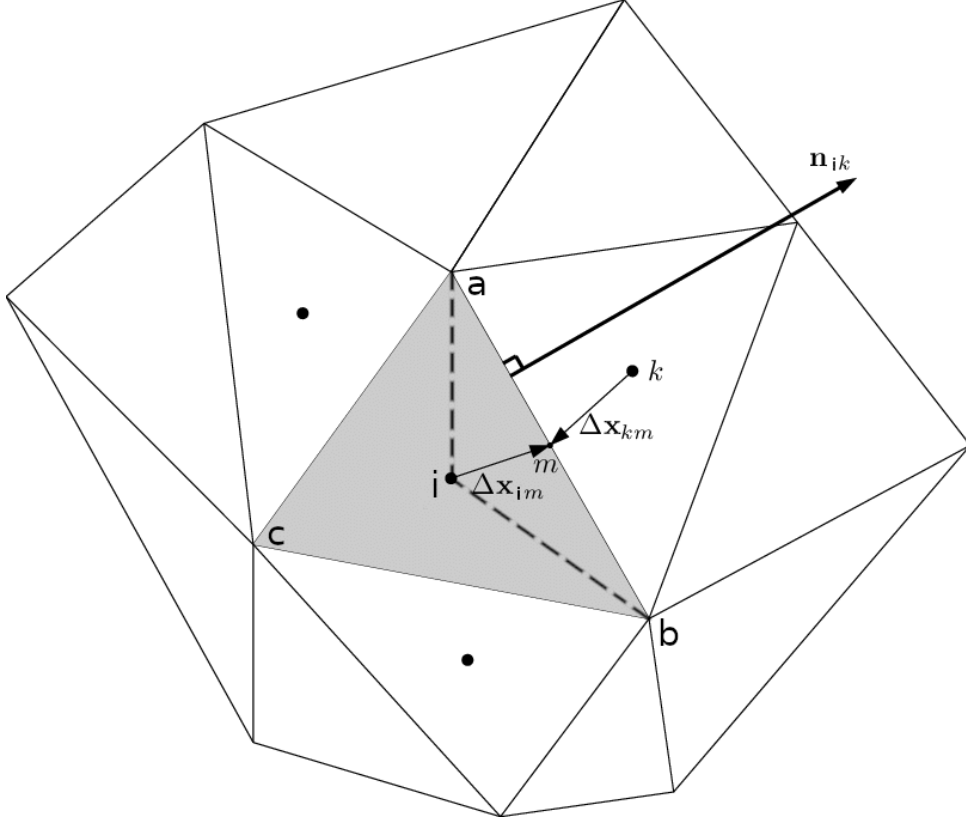


**Figure 1.2.1:** Cell-centered finite volume.

Herein  $(n_x, n_y)$  are the components of the normalized external normal to the edge of the cell. The physical interpretation of this results is the following. In an arbitrary domain, the rate of variation of the conservative variables  $U$  is given by the net flux towards the inside of the cell plus the variation generated by the source term.

The mesh is supposed to be freezed in space and the coordinates of the nodes are time-invariant. The temporal derivative is constant inside the cells and can go out of the surface integral. The previous result becomes

$$\frac{\partial U_i}{\partial t} = -\frac{1}{\Omega_i} \oint_{\Gamma_i} (n_x F(U) + n_y G(U)) d\Gamma_i + \frac{1}{\Omega_i} \int_{\Omega_i} gh(S_0 + S_f) d\Omega_i \quad (1.9)$$

The discretization of the temporal term, the flux terms and the source term are set in the next three sections. The reader is referred to Fig. 1.2.1 for the definition of the geometrical inputs required by the cell-centered finite volume method.

### 1.2.2 Definition of the discretized flux

The line integral in Eq. (1.9) is split in a sum of integrals along each edge  $\Gamma_{ik}$  of the cell. In Fig. 1.2.1, the edges  $\Gamma_{ik}$  are the edges  $abc$ . Index  $i$  denotes the current cell and index  $k$  denotes the cell located on the other side of the edge  $\Gamma_{ik}$ .

$$\oint_{\Gamma_i} (n_x F(U) + n_y G(U)) d\Gamma_i = \sum_{k=1}^3 \oint_{\Gamma_{ik}} (n_x^{ik} F(U) + n_y^{ik} G(U)) d\Gamma_i \quad (1.10)$$

The sum is now expressed in terms of the variables at cells  $i$  and  $k$  using an upwind scheme. The van Leer Q-scheme [4] as implemented by Bermúdez [5]. Let us denote the two-dimensional flux

$Z$  as

$$Z(U, n) = n_x F(U) + n_y G(U) \quad (1.11)$$

Then the Q-schemes are a family of upwind schemes in which the numerical flux through the edge  $ik$  is given by

$$\Phi_{ik}(U_i, U_k, n_{ik}) = \frac{Z(U_i, n_{ik}) + Z(U_k, n_{ik})}{2} - \frac{1}{2} |Q(U_m, n_{ik})| (U_k - U_i) \quad (1.12)$$

where  $U_i$ ,  $U_k$  and  $U_m$  are the variables at cells  $i$ ,  $k$  and the intermediate state  $U_m = (U_i + U_k)/2$ . The matrix  $Q$  is the Jacobian matrix of flux and is estimated at the intermediate state  $U_m$ .

$$\begin{aligned} Q &= \frac{dZ}{dU} = n_x \frac{dF}{dU} + n_y \frac{dG}{dU} \\ &= \begin{pmatrix} 0 & n_x & n_y \\ n_x(-u^2 + gh) - n_y(uv) & 2n_x u + n_y v & n_y u \\ -n_x(uv) + n_y(-v^2 + gh) & n_x v & n_x u + 2n_y v \end{pmatrix} \end{aligned} \quad (1.13)$$

The system of equations is hyperbolic in the sense that the Jacobian matrix  $Q$  has real eigenvalues and a complete set of eigenvectors. Matrix  $|Q|$  is obtained by

$$|Q| = X |\Lambda| X^{-1} \quad (1.14)$$

where  $X^{-1}$  is the matrix whose  $j$ th column is the  $j$ th right eigenvector of matrix  $Q$ .  $\Lambda$  is a diagonal matrix containing the absolute values of the eigenvalues  $\lambda_l$  ( $l = 1, 3$ ). Let us denote  $c = \sqrt{gh}$  the speed of the wave. The eigenvalues of the Jacobian matrix are

$$\begin{aligned} \lambda_1 &= n_x u + n_y v \\ \lambda_2 &= \lambda_1 + c \\ \lambda_3 &= \lambda_1 - c \end{aligned} \quad (1.15)$$

$\lambda_2$  and  $\lambda_3$  are gravity waves while  $\lambda_1$  is linearly degenerate.  $|\Lambda|$ ,  $X$  and  $X^{-1}$  can be calculated

$$|\Lambda| = \begin{pmatrix} |\lambda_1| & 0 & 0 \\ 0 & |\lambda_2| & 0 \\ 0 & 0 & |\lambda_3| \end{pmatrix} \quad (1.16)$$

$$X = \begin{pmatrix} 0 & 1 & 1 \\ -n_y c & u + n_x c & u - n_x c \\ n_x c & v + n_y c & v - n_y c \end{pmatrix} \quad (1.17)$$

$$X^{-1} = \frac{1}{2c} \begin{pmatrix} 2(n_y u - n_x v) & -2n_y & 2n_x \\ c - n_x u - n_y v & n_x & n_y \\ c + n_x u + n_y v & -n_x & -n_y \end{pmatrix} \quad (1.18)$$

Finally the line integral (1.10) can be discretized by

$$\begin{aligned} \oint_{\Gamma_i} (n_x F(U) + n_y G(U)) d\Gamma_i &= \sum_{k=1}^3 \oint_{\Gamma_{ik}} (n_x^{ik} F(U) + n_y^{ik} G(U)) d\Gamma_i \\ &\approx \sum_{k=1}^3 \Phi_{ik} L_{ik} \end{aligned} \quad (1.19)$$

where  $L_{ik}$  is the length of the edge between cells  $i$  and  $k$ .

### 1.2.3 Definition of the discretized source

#### 1.2.3.1 Geometric slope

The contribution of the geometric slope to the surface integral of the source term in Eq. (1.9) is split in a sum of integrals over the three subcells  $iab$ ,  $ibc$  and  $ica$ .

$$\int_{\Omega_i} ghS_0 d\Omega_i \approx \sum_{k=1}^3 \varphi_{ik} \Omega_{ik} \quad (1.20)$$

The terms  $\varphi_{ik}$  and  $\Omega_{ik}$  are respectively the approximated source term within each subcell and the area of these subcells. The convenience of upwinding the source term has been analyzed by Castro [6]. This use of this technique was justified in the case of one-dimensional problems as a means to avoid the propagation of spurious waves. In some sense, it was shown that the discretization of the source term should mimic that of the flux. The two-dimensional source in the three subcells  $iab$ ,  $ibc$  and  $ica$  is approximated by

$$\varphi_{ik} = X(I - |\Lambda| \Lambda^{-1})X^{-1} \hat{S}_0 \quad (1.21)$$

Matrix  $I$  is the  $3 \times 3$  identity matrix. Matrices  $X$ ,  $X^{-1}$ ,  $|\Lambda|$  and  $\Lambda^{-1}$  are evaluated at the intermediate state  $U_m$ . The inverse eigenvalue matrix is given by

$$\Lambda^{-1} = \begin{pmatrix} 1/\lambda_1 & 0 & 0 \\ 0 & 1/\lambda_2 & 0 \\ 0 & 0 & 1/\lambda_3 \end{pmatrix} \quad (1.22)$$

The term  $|\Lambda| \Lambda^{-1}$  is thus equivalent to  $sign(\Lambda)$ , the matrix whose coefficients are the sign of the eigenvalues of matrix  $Q$ . The geometric source term  $\hat{S}$  is approximated by

$$\hat{S}_0 \approx gh_m \frac{z_b^i - z_b^k}{\Delta x_{im}} \begin{pmatrix} 0 \\ n_x \\ n_y \end{pmatrix} \quad (1.23)$$

where  $\Delta x_{im}$  is the distance between the cell center  $i$  and the mid-node  $m$  and  $z_b^i$ ,  $z_b^k$  are the heights of the ground at cells  $i$  and  $k$ .

#### 1.2.3.2 Friction slope

The contribution of the friction slope to the surface integral of the source term in Eq. (1.9) as given in Eq. (1.4) is evaluated by averaging the friction term over the cell:

$$\int_{\Omega_i} ghS_f d\Omega_i \approx -gh_i \sqrt{u_i^2 + v_i^2} \frac{n_b^2}{h_i^{4/3}} \Omega_i \begin{pmatrix} 0 \\ u_i \\ v_i \end{pmatrix} \quad (1.24)$$

The discretization of the extension of the Manning formula to take into account the wall friction (1.5) is given by

$$\int_{\Omega_i} ghS_f d\Omega_i \approx -gh_i \sqrt{u_i^2 + v_i^2} \left( \frac{n_b^{3/2}}{h_i} + \sum_{j=1}^3 \frac{\mu_{ij} n_w^{3/2} l_j}{\Omega_i} \right)^{4/3} \Omega_i \begin{pmatrix} 0 \\ u_i \\ v_i \end{pmatrix} \quad (1.25)$$

Herein  $\mu_{ij}$  equals 1 if side  $j$  of cell  $i$  is a wall, and equals 0 otherwise.  $l_j$  is the length of side  $j$ .

### 1.2.4 Extension to order 2 in space (MUSCL)

In order to improve the accuracy of the basic first order scheme a piecewise linear reconstruction of the solution is used within each cell. The method used here is the MUSCL (monotone upstream scheme for conservation law) scheme introduced by van Leer who generalized the original Godunov's method. Through this method TVD (total variation diminishing) schemes are enabled. The main advantage of the MUSCL scheme is that it keeps a high order of precision in the whole domain except near the discontinuities, where the reconstruction is switched off. The implementation within the current code follows the one proposed by Sahmim [7].

At the middle point  $m$  of the edge  $ab$  that delimits cells  $i$  and  $k$  (see Fig.1.2.1), two reconstructed values are defined on each side of the edge:  $U_{ik}^-$  inside cell  $i$  and  $U_{ik}^+$  inside cell  $k$

$$\begin{aligned} U_{ik}^- &= U_i + \frac{1}{2} \bar{\nabla} U_i \overline{G_i G_k} \\ U_{ik}^+ &= U_k - \frac{1}{2} \bar{\nabla} U_k \overline{G_i G_k} \end{aligned} \quad (1.26)$$

In the previous relation  $U_i$  and  $U_k$  are the cell values of the solution (either  $h$ ,  $hu$  or  $hv$ ),  $\bar{\nabla} U_i$  and  $\bar{\nabla} U_k$  are the cell gradients within both cells and  $\overline{G_i G_k}$  is the vector that joins both centers of the cells. Let's underline that the definition of the fluxes has given in the previous sections remain identical with the exception that  $U_i$  is replaced by  $U_{ik}^-$  and  $U_k$  by  $U_{ik}^+$ .

The crucial part of the MUSCL method is the computation of the gradient  $\bar{\nabla} U$  within each cell. The method proposed by Sahmim [7] has the advantage to be applicable on both triangular and quadrangular cells. The gradient within cell  $i$  is given by

$$\frac{\partial U_i}{\partial x} = \frac{J_x I_{yy} - J_y I_{xy}}{D} \quad \frac{\partial U_i}{\partial y} = \frac{J_y I_{xx} - J_x I_{xy}}{D} \quad (1.27)$$

where

$$\begin{aligned} I_{xx} &= \sum_{k \in N(i)} (x_k - x_i)^2 & I_{yy} &= \sum_{k \in N(i)} (y_k - y_i)^2 \\ I_{xy} &= \sum_{k \in N(i)} (x_k - x_i)(y_k - y_i) & D &= I_{xx} I_{yy} - I_{xy}^2 \\ J_x &= \sum_{k \in N(i)} (x_k - x_i)(U_k - U_i) & J_y &= \sum_{k \in N(i)} (y_k - y_i)(U_k - U_i) \end{aligned}$$

In the previous relations  $N(i)$  is the set of cells  $k$  that surrounds cell  $i$ ,  $(x_i, y_i)$  and  $(x_k, y_k)$  are the coordinates of the centers of cells  $i$  and  $k$  respectively. The reconstructed solution at the middle of the edges can still show spurious oscillations near regions of rapid variation. Therefore the gradients given in Eq.(1.27) must be limited to preserve a TVD scheme. The reconstructed values at the middle of the edge given in Eq.(1.26) are thus replaced by

$$\begin{aligned} U_{ik}^- &= U_i + \frac{1}{2} \bar{\nabla}^{lim} U_i \overline{G_i G_k} \\ U_{ik}^+ &= U_k - \frac{1}{2} \bar{\nabla}^{lim} U_k \overline{G_i G_k} \end{aligned} \quad (1.28)$$

where the limited gradient is expressed by

$$\frac{\partial^{lim} U_i}{\partial x} = \frac{1}{2} \left[ \min_{k \in N(i)} \text{sign} \left( \frac{\partial U_k}{\partial x} \right) + \max_{k \in N(i)} \text{sign} \left( \frac{\partial U_k}{\partial x} \right) \right] \min_{k \in N(i)} \left| \frac{\partial U_k}{\partial x} \right| \quad (1.29)$$

and a similar expression for  $\partial^{lim} U_i / \partial y$

### 1.2.5 Boundary conditions

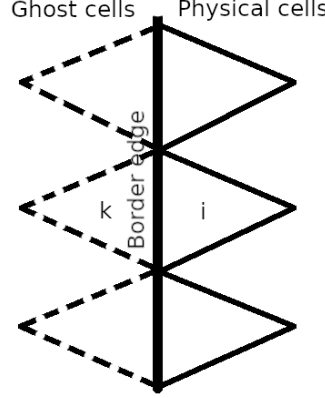


**Figure 1.2.2:** Definition of the ghost cells for imposing the boundary conditions.

The characteristic waves that propagate inside the domain have the Eigenvalues (1.15) as slopes. The number of incoming characteristics determine the number of boundary conditions to be set at each boundary edge. The flow regime (or the Froude number as defined in Eq. (1.6)) determines the number of incoming characteristics for each set of boundary edge. Knowing the number of imposed boundary conditions is a first step. A second step is the actual way to impose these conditions. In the finite volume methods, it is common to resort to *ghost cells* (see Fig.1.2.2) which will help to compute the required flux at the boundary edges. These ghost cells are artificial cells located on the other side of the border edge. They contain values  $U_k$  calculated in a way that the mean flux at the boundary edge is based on the imposed boundary values  $U_{BC}$ :

$$\Phi_{ik}(U_i, U_k, n_{ik}) = \frac{Z(U_i, n_{ik}) + Z(U_k, n_{ik})}{2} = Z(U_{BC}, n_{ik}) \quad (1.30)$$

These ghost cells have the same area as the physical cells attached to the common boundary edge. The upwinding method is applied for the flux but not for the source term. In the next subsections, it is supposed that  $\lambda_1 > 1$ , meaning that the flow enters for an inflow boundary and exits for an outflow boundary.

#### 1.2.5.1 Inflow boundary condition

- A subcritical inflow has two incoming characteristics ( $\lambda_1$  and  $\lambda_2$  being positive and  $\lambda_3$  being negative), and thus two boundary values must be imposed at the edge. These two values are chosen as the two components of the velocity vector  $(u_{BC}, v_{BC})$ . Thus the ghost cells contain the values

$$h_k = h_i \quad u_k = 2u_{BC} - u_i \quad v_k = 2v_{BC} - v_i$$

- A supercritical inflow has three incoming characteristics, and thus three boundary values must be imposed at the edge. These three values are chosen as the height  $h_{BC}$  and the two components of the velocity vector  $(u_{BC}, v_{BC})$ . Thus the ghost cells contain the values

$$h_k = 2h_{BC} - h_i \quad u_k = 2u_{BC} - u_i \quad v_k = 2v_{BC} - v_i$$



### 1.2.5.2 Outflow boundary condition

- A subcritical outflow has one incoming characteristics ( $\lambda_3$ ), and thus one boundary value must be imposed at the edge. This value is chosen as the the height  $h_{BC}$ . Thus the ghost cells contain the values

$$h_k = 2h_{BC} - h_i \quad u_k = u_i \quad v_k = v_i$$

- A supercritical outflow has zero incoming characteristics, and thus no boundary condition is imposed. The ghost cells contain the values

$$h_k = h_i \quad u_k = u_i \quad v_k = v_i$$

### 1.2.5.3 Slip-wall boundary condition

A slip-wall condition cancels the wall-normal velocity component and the velocity vector is parallel to the edge. Thus the ghost cells contain the values

$$h_k = h_i \quad u_k = u_i - 2(un_x + vn_y)n_x \quad v_k = v_i - 2(un_x + vn_y)n_y$$

### 1.2.5.4 Symmetry boundary condition

A symmetry boundary condition mirrors the values in cell  $i$ . Thus the ghost cells contain the values

$$h_k = h_i \quad u_k = -u_i \quad v_k = -v_i$$

## 1.2.6 Definition of the discretized time derivative

The spatial discretization of the flux  $\Phi_{ik}$  and source  $\varphi_{ik}$  terms described in the two previous sections led Eq. (1.9) to the following result:

$$\frac{\partial U_i}{\partial t} = \frac{1}{\Omega_i} \left( \sum_{k=1}^3 -\Phi_{ik} L_{ik} + \varphi_{ik} \Omega_{ik} \right) \quad (1.31)$$

$$= f(U, t) \quad (1.32)$$

Two time integration algorithms are implemented in the solver: the well-known fourth-order explicit Runge-Kutta method and the third order Total Variation Diminishing (TVD) explicit Runge-Kutta method.

### 1.2.6.1 Fourth-order explicit Runge-Kutta method

This method allows to reach a high accuracy in time while having a limit on the Courant-Friedrich-Lewy number (defined in Eq. (1.33)) which is higher than other standard methods.

$$\text{CFL} = \frac{\max(u)\Delta t}{\Delta x} \lesssim 2.8 \quad (1.33)$$

In the case of a generic equation  $\partial U_i / \partial t = f(U, t)$ , the RK4 time integrator provides the next time step solution through

$$\begin{aligned} k_1 &= \Delta t f(U^n, t^n) \\ k_2 &= \Delta t f\left(U^n + \frac{k_1}{2}, t + \frac{\Delta t}{2}\right) \end{aligned}$$

$$\begin{aligned}
k_3 &= \Delta t f(U^n + \frac{k_2}{2}, t + \frac{\Delta t}{2}) \\
k_4 &= \Delta t f(U^n + k_3, t + \Delta t) \\
U^{n+1} &= U^n + \frac{1}{6}(k_1 + 2k_2 + 2k_3 + k_4)
\end{aligned} \tag{1.34}$$

### 1.2.6.2 Third order TVD explicit Runge-Kutta method

In Shu [8] a general TVD Runge-Kutta method is written under the form

$$U^{(i)} = \sum_{k=0}^{i-1} \left[ \alpha_{ik} U^{(k)} + \beta_{ik} \Delta t f(U^{(k)}) \right], \quad i = 1, m \tag{1.35}$$

The optimal third order scheme ( $m = 3$ ) is given by

$$\begin{aligned}
U^{(1)} &= U^n + \Delta t f(U^n) \\
U^{(2)} &= \frac{3}{4}U^n + \frac{1}{4}U^{(1)} + \frac{\Delta t}{4}f(U^{(1)}) \\
U^{n+1} &= \frac{1}{3}U^n + \frac{2}{3}U^{(2)} + \frac{2}{3}\Delta t f(U^{(2)})
\end{aligned} \tag{1.36}$$

The coefficients  $\alpha_{ik}$  and  $\beta_{ik}$  are all positive, which ensures that the scheme is effectively TVD. Another clear advantage of this method is the low storage required to evaluate each substep.

### 1.2.7 Local time stepping

In case of steady flows, a local time stepping method is useful to accelerate the convergence towards the steady solution. The chosen local time step method within each cell is

$$\Delta t = \frac{\Omega \text{ CFL}}{\sum_{j=1}^3 |un_x^j + vn_y^j| + cL} \tag{1.37}$$

where  $\Omega$  is the area of the cell,  $(u, v)$  are the velocity components,  $c = \sqrt{gh}$  is the wave speed,  $L$  is the perimeter of the cell and CFL is the Courant-Friedrich-Lewy number (defined in Eq. (1.33)).

## Chapter 2

# Verification of the code

### 2.1 Straight channel with slope and bottom friction

A straight channel with bottom slope and friction is first compared with the theoretical solution from gradually-varied flows in open channels. The width of the channel is  $B_0 = 2m$ , its length is  $L = 1000m$  and its cross-section is rectangular. The mesh is composed of  $1m$ -side long right-angled triangles with a total of 4000 cells. The unit discharge is  $q = Q/B_0 = 4m^2/s$  and two flow configurations (mild and steep slopes) were considered.

The numerical results are compared with the curves of the theory of gradually-varied flows in open channels. The reader is referred to Chow [2] and Chaudhry [9] for this theory. Two important parameters that drive the behaviour of the flow are the normal depth  $y_n$  and the critical depth  $y_c$ . The last one depends only on the geometry of the channel and is calculated through

$$y_c = \sqrt[3]{\frac{q^2}{g}} \quad (2.1)$$

The normal depth  $y_n$  is calculated in an iterative process by

$$Q = qB_0 = VA = \frac{A}{n}R^{2/3}\sqrt{S_0} \quad (2.2)$$

where  $R = A/P$  is the hydraulic radius,  $A = B_0y_n$  is the cross-section area  $P = B_0 + 2y_n$  is the wetted perimeter. The inputs of this equation are the Manning coefficient of roughness  $n$ , the geometrical slope  $S_0$ , the channel bottom width  $B_0$  and the unit discharge  $q$ . The water level is also calculated in an iterative process by imposing a water level at one extremity of the channel and by computing the water slope with

$$\frac{dh}{dx} = \frac{S_0 - S_f}{1 - \frac{Q^2 B_0}{g A^3}} \quad (2.3)$$

where the friction slope  $S_f = n^2 V^2 / R^{4/3}$ . The standard step method described in Chow [2] and Chaudhry [9] is used to determine the water level at specified locations.

In the present configuration, it has been decided to neglect the friction coefficient of the side walls  $n_w$  and to keep only the friction at the bottom of the channel  $n_b$ . Indeed imposing a non zero friction coefficient  $n_w$  at the walls will induce subcritical areas in a globally supercritical flow. This will complicate the imposition of the boundary conditions at the exit (what value to impose for the height in these subcritical areas at the exit?) and the comparison with the theoretical curves (compare the theory with the average height profiles or at the centerline?). Therefore, in the following, a Manning coefficient  $n_b$  is chosen for the 2D computations and a

Mild slope		$n_b$	$y_n$	$y_c$
	2D shallow water	0.015	1.579m measured	1.1771m
	1D	0.015	2.394m	1.1771m
	1D with $n_e$	0.0082	1.4686m	1.1771m
	1D with $n_e$ manual	0.009	1.579m	1.1771m
Steep slope		$n_b$	$y_n$	$y_c$
	2D shallow water	0.01	1.004m measured	1.1771m
	1D	0.01	1.306m	1.1771m
	1D with $n_e$	0.0067	0.9353m	1.1771m
	1D with $n_e$ manual	0.00708	1.004m	1.1771m

**Table 2.1:** Straight channel with slope and bottom friction - Values for  $n_b$ ,  $y_c$  and  $y_n$  for the 1D and 2D computations.

Manning coefficient  $n$  must be found so that the normal depths of both models match. Cueto-Felgueroso [10] compared 1D and 2D computations and also adapted the Manning coefficient for the 1D model. An equivalent Manning coefficient is calculated through

$$n_e = \left( \frac{\sum P_i n_i^{3/2}}{\sum P_i} \right)^{2/3} = \left( \frac{B_0 n^{3/2}}{B_0 + 2y_n} \right)^{2/3} \quad (2.4)$$

The equivalent Manning coefficient is then used in conjunction with  $y_n$  in the iterative process of Eq. (2.2) and the water level through the standard step method. The calculated values are given in Table 2.1.

The two flow regimes calculated are based on the following parameters

- Mild slope  $y_n > y_c$ : the geometrical slope is  $S_0 = 0.001$  and the Manning coefficient  $n_b = 0.015$  for the 2D computations. For the theoretical 1D computation, the Manning coefficient must be adapted because the effect of friction is not taken into account along the side walls of the channel in the current implementation of the 2D shallow water solver ( $n = 0$  along the walls). The Manning coefficient  $n_b = 0.015$  used in the 2D solver leads to a too big theoretical  $y_n$  (in comparison with the measured one in the 2D solver). The equivalent Manning coefficient  $n_e$  calculated through Eq. (2.4) improved  $y_n$  but the difference is still too important. The manually chosen value  $n_e = 0.009$  leads to the best fit between 1D and 2D and this value will be used for the 1D computation.

As discussed in Section 1.2.5, subcritical flows are calculated by imposing the unit discharge  $q$  at the inlet and the water height  $h_{BC}$  at the outlet. Two cases are explored: case 1 with an imposed height  $h_{BC} = 1.75m > y_n$  and case 2 with an imposed height  $y_c < h_{BC} = 1.2m < y_n$ . Doing so the mild-slope profiles M1 and M2 are selected. The supercritical profile M3 is not selected because it appears mostly behind partially opened sluice gates.

- Steep slope  $y_n < y_c$ : the geometrical slope is  $S_0 = 0.002$  and the Manning coefficient  $n_b = 0.01$  for the 2D computations. The Manning coefficient  $n_b = 0.01$  used in the 2D solver leads to a too big theoretical  $y_n$  (in comparison with the measured one in the 2D solver). The equivalent Manning coefficient  $n_e$  calculated through Eq. (2.4) improved  $y_n$  but the difference is still too important. The manually chosen value  $n_e = 0.00708$  leads to the best fit between 1D and 2D and this value will be used for the 1D computation.

Three cases are explored: the subcritical case 3 with an imposed height  $h_{BC} = 3.4m > y_c$  at the outlet and the supercritical cases 4 and 5 with an imposed height  $y_n < h_{BC} =$

$1.15m < y_c$  and  $h_{BC} = 0.7m < y_n$  respectively. The subcritical case 3 corresponds to the profile S1 and the supercritical cases 4 and 5 correspond to the profiles S2 and S3.

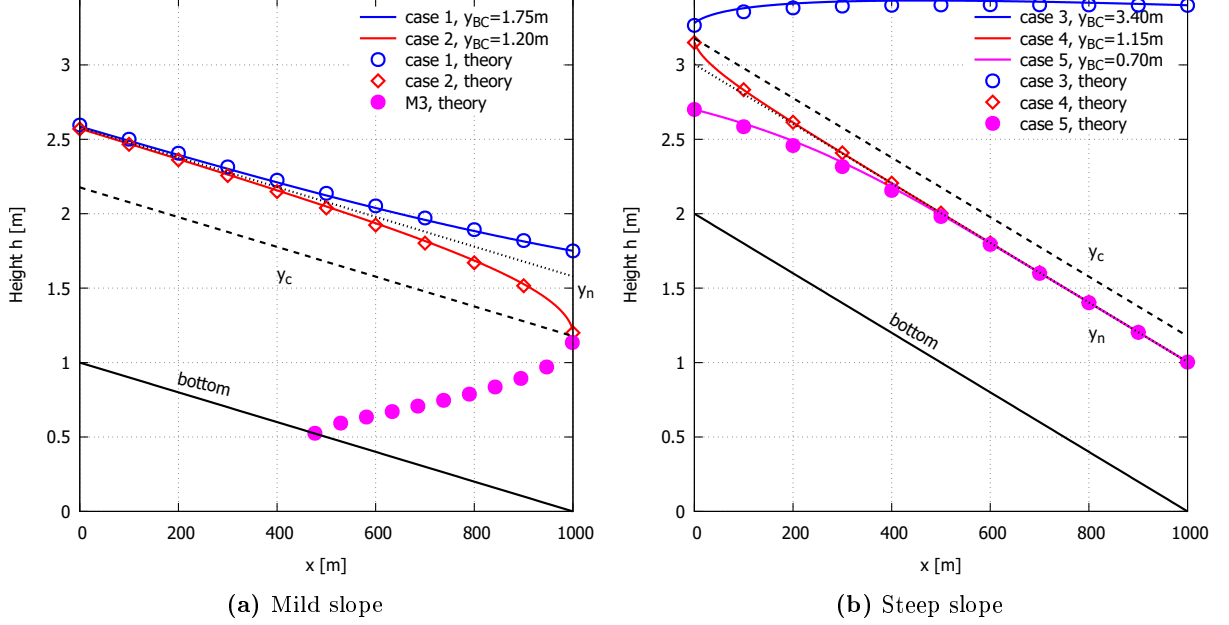


**Figure 2.1.1:** Straight channel with slope and bottom friction - Water levels in the case of a (left) mild slope and (right) steep slope. Comparison with the theoretical curves. The normal depth  $y_n$  and the critical depth  $y_c$  are depicted by dotted and dashed lines respectively

The water level at the centerline of the channel is plotted in Fig. 2.1.1 for both mild and steep slopes. A perfect matching with the theoretical curves is observed in every considered case. The normal depth is reached asymptotically whereas the critical depth is reached vertically. The water level in case 3 (=S1) tends to an horizontal asymptote. Indeed the analysis of Eq. (2.3) shows that for  $h \rightarrow \infty$  then  $Q \rightarrow 0$  and  $S_f \rightarrow 0$  will means that  $dh/dx \rightarrow S_0$ . The theoretical supercritical profile M3 as been plotted in the case where  $y_{BC} = 1.15m < y_c$ . It is clear that such a profile can be computed by the shallow water solver only if the channel length  $L < 523.2m$ , location where the water level reaches the bottom of the channel. Case 3 has been particularly difficult to converge because of the upstream influence of the imposed water height. During the computation, the calculated water height at the inlet oscillated above and below the critical depth, changing the inlet from a supercritical to a subcritical boundary condition.

An important criteria to be respected by the numerical discretization is the conservation of the flowrate  $Q$  throughout the channel. Figure 2.1.2 shows the unit discharge  $q = hu$  extracted from cuts perpendicular to the flow for the five cases. The maximum deviation from the nominal unit discharge is less than 0.5%, which shows a very good conservation of the flowrate.

This benchmark has allowed to validate the correct implementation of the source terms (both the geometrical and the friction slopes). This benchmark did not put forward any hydraulic jump where an important variation in height occurs in a short distance. Thus the stability of the Q-scheme has not been tested yet.

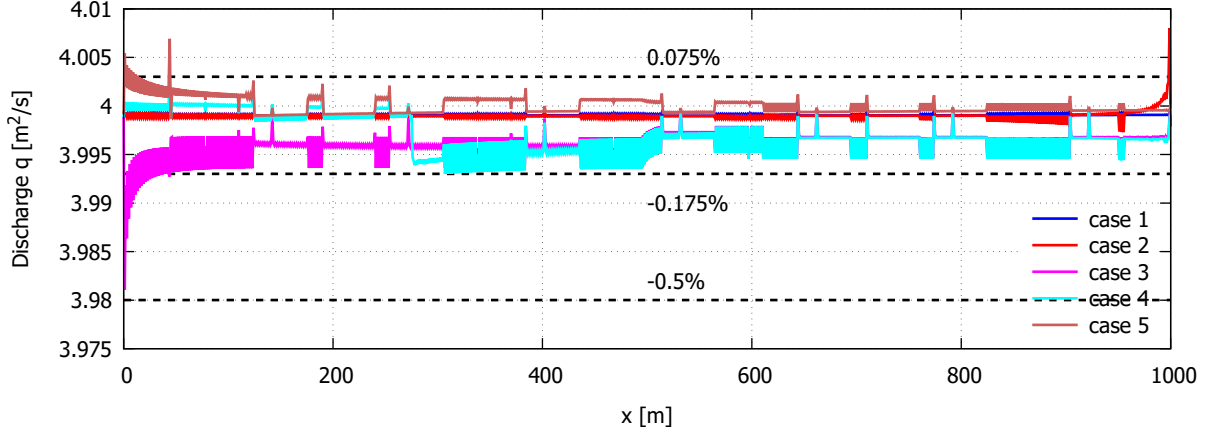


**Figure 2.1.2:** Straight channel with slope and bottom friction - Discharge  $q = Q/B_0$  along the channel.

## 2.2 Straight channel with slope, bottom and wall friction

This section considers the same configuration as in the previous one with the addition of the side wall friction term (Eq. (1.5)). Now both the bottom  $n_b$  and side walls  $n_w$  Manning coefficients are taken into account by activating the corresponding parameters. The addition of friction along the walls will create a boundary layer-like behaviour. Thus the mesh must be adapted to this situation by increasing the number of elements along the direction perpendicular to the flow. The flow configuration is chosen similar to case 5 in Section 2.1. The flow will remain supercritical in overall with the exception of the subcritical region near to the walls. The width and length of the channel are  $B_0 = 2m$  and  $L = 1000m$ , the geometrical slope is  $S_0 = 0.002$ , the unit discharge  $q = Q/B_0 = 4m^2/s$ , the Manning coefficients for the 2D computations are  $n_b = n_w = 0.01$ . At the inlet one imposes  $h_{inlet} = 0.75m$  (supercritical) and at the outlet  $h_{outlet} = 1.163235m$ . This last value is active for the subcritical area near the side walls only. The theoretical curve for the height matches best the 2D results for  $n_{th} = 0.0086$  (which is more comparable to the 2D value than in Section 2.1). This Manning coefficient for the 1D computation leads to a height  $h_{outlet} = 1.163235m$  which was chosen as boundary value for the 2D computation.

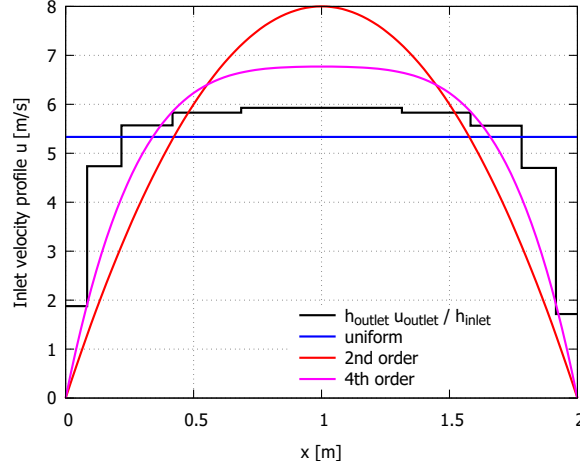
Three cases were considered for the imposition of the velocity profile at the inlet: (case ①) an uniform one, (case ②) a second order one and (case ③) a fourth order velocity profile. Case ① gives directly  $u_{inlet} = q/h_{inlet}$ . Cases ② and ③ integrate the velocity profiles along the transverse direction in order to match the overall unit discharge  $Q = qB_0 = h_{inlet} \int_0^{B_0} u(y)dy$ . The boundary conditions on these profiles are  $u_{inlet}(0) = u_{inlet}(B_0) = 0$  and  $\partial u_{inlet}(B_0/2)/\partial y = 0$ . For case ③ the additional condition is  $\partial^2 u_{inlet}(0)/\partial y^2 = \partial^2 u_{inlet}(B_0)/\partial y^2 = \alpha$  controls the roundness of the profiles. The second order velocity profile is given by

$$u(y) = -\frac{6q}{h_{inlet}B_0^2} (y^2 - B_0y) \quad (2.5)$$

and the fourth order velocity profile by

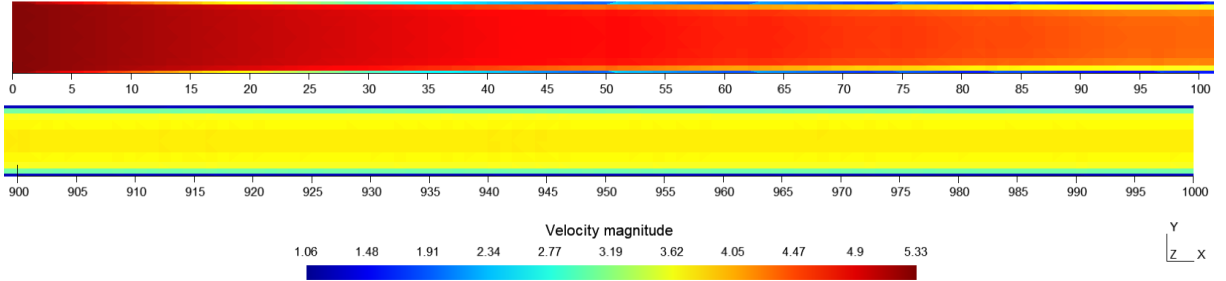
$$\begin{aligned} u(y) &= ay^4 + by^3 + cy^2 + dy \\ a &= \frac{5}{B_0^5} \left( \frac{B_0q}{h_{inlet}} + \frac{\alpha B_0^3}{12} \right) & b &= -2aB_0 \\ c &= \frac{\alpha}{2} & d &= aB_0^3 - \frac{\alpha}{2}B_0 \end{aligned} \quad (2.6)$$

In the previous relation, parameter  $\alpha$  has been chosen equal to  $-75$ . The three velocity profiles used in this configuration are shown in Fig. 2.2.1 as well as the corrected velocity profile extracted at the outlet of case ①.



**Figure 2.2.1:** Straight channel with slope, bottom and wall friction - Several velocity profiles imposed at the inlet. The black line represents the velocity profile from the outlet of the 2D model with uniform inlet corrected for the inlet condition.

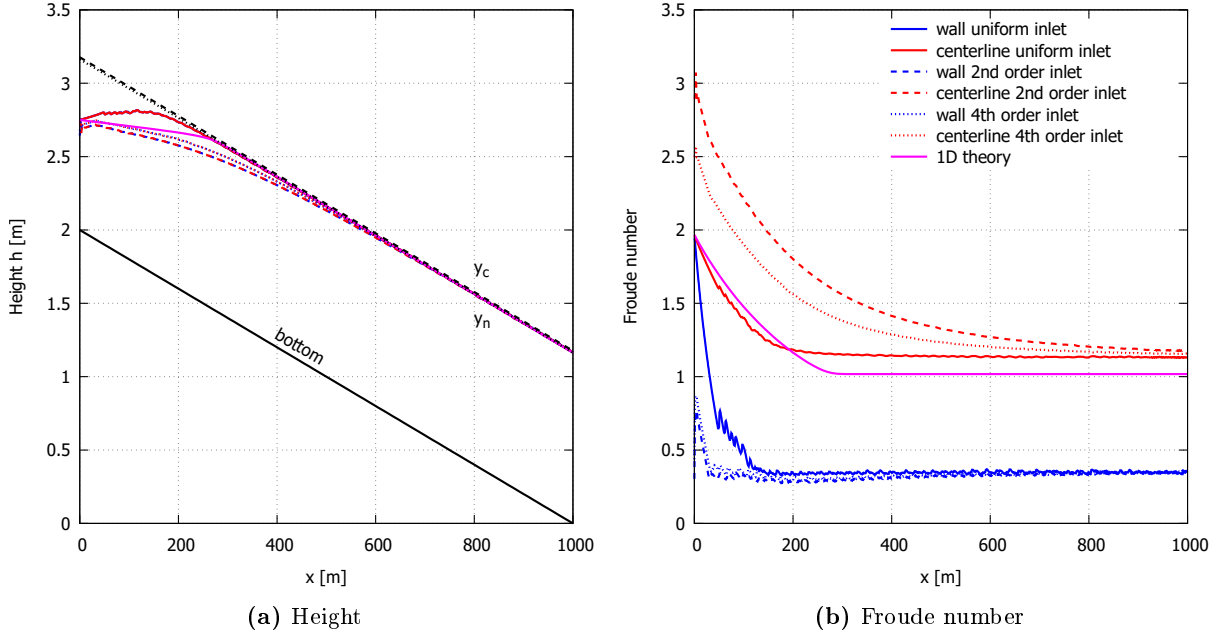
Figure 2.2.2 shows the magnitude of the velocity at the inlet and outlet of the channel for case ①. One clearly sees the progressive development of the boundary layer at the inlet whereas it is completely developed at the outlet.



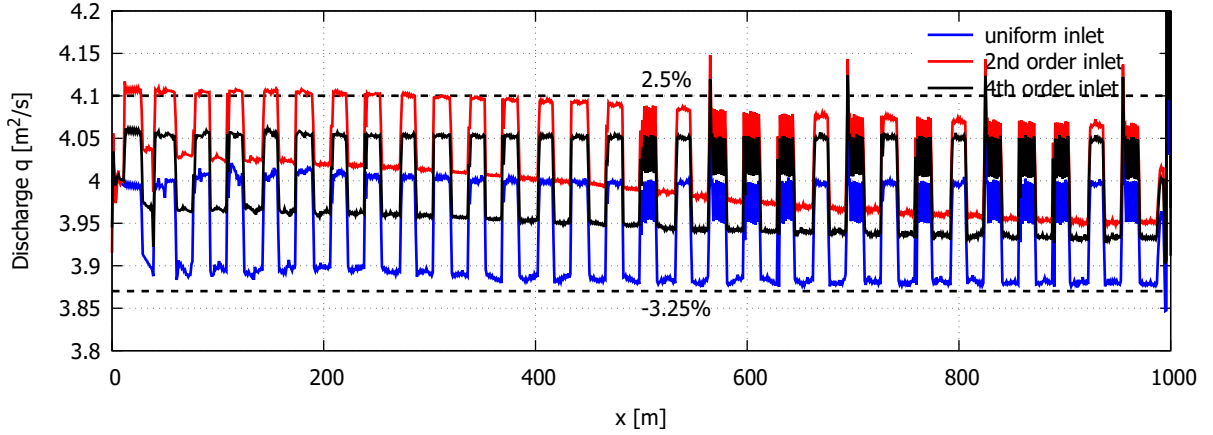
**Figure 2.2.2:** Straight channel with slope, bottom and wall friction - Development of the boundary layer (top) at the inlet and (bottom) at the outlet.

Figure 2.2.3 shows the height and Froude number along cuts at the wall and at the centerline. The theoretical 1D curves are also depicted for comparison. The height is more or less uniform along the direction perpendicular to the flow. Because of the variation of the velocity profile and because the unit discharge must be conserved, the Froude number also displays a varying shape along the direction perpendicular to the flow. A subcritical area is indeed observed near the wall and a supercritical core allows to ensure the conservation of the flow rate. For case ① a very good agreement is reached for the height after that the boundary layer has been developed ( $x > 200m$ ). In the region  $x < 200m$ , the water level predicted by the 2D model overshoots the theoretical one because of the global deceleration of the flow. An unsteadiness also appears, triggered by fluctuations inside the boundary layer. Cases ② and ③ do not show the overshoot at the beginning of the channel but are slower to converge towards the theoretical value. The Froude number converges faster than case ① at the wall but slower at the centerline.

In opposition to the case where the side wall friction was neglected, the evolution of the



**Figure 2.2.3:** Straight channel with slope, bottom and wall friction - (left) Water levels and (right) Froude number. Comparison with the theoretical curves. The normal depth  $y_n$  and the critical depth  $y_c$  are depicted by dotted and dashed lines respectively



**Figure 2.2.4:** Straight channel with slope, bottom and wall friction - Discharge  $q = Q/B_0$  along the channel.

flowrate along the channel shows a more pronounced deviation from the imposed value (see Fig. 2.2.4). Case ① shows an error between -3.25% and 0.5%, case ② shows an error between -1.25% and 2.5% and case ③ shows a more symmetrical error between -1.25% and 1.25%.

## 2.3 Oblique hydraulic jump

A supercritical flow is deflected inwards by a vertical boundary (slope  $\theta$ , see Fig.2.3.1). No bathymetric variation is present in the flow. Slip-wall boundary conditions are imposed on the top and bottom parts of the flow. The initial height of the flow  $h_1$  increases abruptly to a height  $h_2$  along a wavefront which extends from the point of boundary discontinuity  $C$  at a wave angle



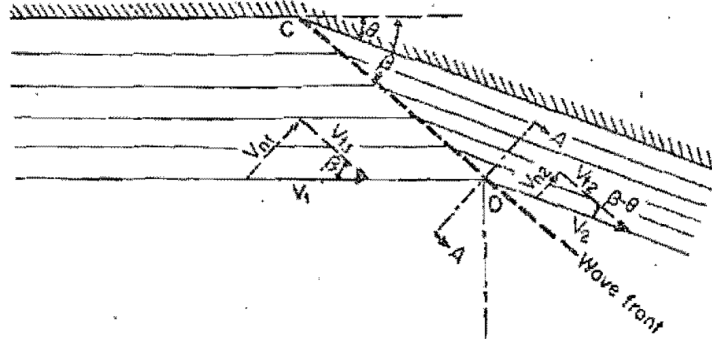


**Figure 2.3.1:** Oblique hydraulic jump

$\beta$ . The magnitude of  $\beta$  depends partially on the angle  $\theta$ . When  $\theta = 0$ , one retrieves the normal hydraulic jump with the wavefront perpendicular to the direction of flow ( $\beta = 90$  deg). By imposing values for  $\theta$  and the Froude number  $Fr_1 = v_1/\sqrt{gh_1}$  upstream of the jump, the wave angle  $\beta$  can be calculated by iteration on the following relation (see Chow [2]):

$$\tan \theta = \frac{\tan \beta \left( \sqrt{1 + 8Fr_1^2 \sin^2 \beta} - 3 \right)}{2 \tan^2 \beta + \sqrt{1 + 8Fr_1^2 \sin^2 \beta} - 1} \quad (2.7)$$

Then the height  $h_2$  and the amplitude of the velocity  $u_2$  downstream of the jump can be retrieved by the relations

$$h_2 = h_1 \frac{\tan \beta}{\tan (\beta - \theta)} \quad (2.8)$$

$$v_2 = v_1 \frac{\cos \beta}{\cos (\beta - \theta)} \quad (2.9)$$

Yoon and Kang [11] and Valiani *et al.* [12] also used this test case as a benchmark for their codes.

The inflow Froude number is chosen in a way that the flow remains supercritical behind the jump. The chosen flow parameters are

$$\theta = 10 \text{ deg} \quad h_1 = 1.0 \quad u_1 = 9.0 \quad Fr_1 = 2.8735 \quad (2.10)$$

With the help of Eqs. (2.7)- (2.9), this leads to

$$\beta = 29.882 \text{ deg} \quad h_2 = 1.5889 \quad u_2 = 8.2981 \quad Fr_2 = 2.1018 \quad (2.11)$$

A set of uniform meshes of triangles are built, see Fig. 2.3.2 for one example. The horizontal and vertical sides of the triangles on the inflow boundary have the same length. This length is used as the characteristic length of the mesh during the study of the convergence rate later in this section. The wavefront will cut through cells so that a region of transition will exist between the upstream and downstream solutions. As the solution is steady, a local time step is calculated for each cell.

The left part of Fig. 2.3.3 shows the converged height when the MUSCL scheme is deactivated. Two major observations can be made. First the solution is homogeneous upstream and downstream of the jump. Secondly the location of the wavefront coincides with the theoretical one. A region of transition exists around the wavefront because the wavefront cuts through the cells. No spatial oscillation is observed inside the solution, specially around the wavefront. The

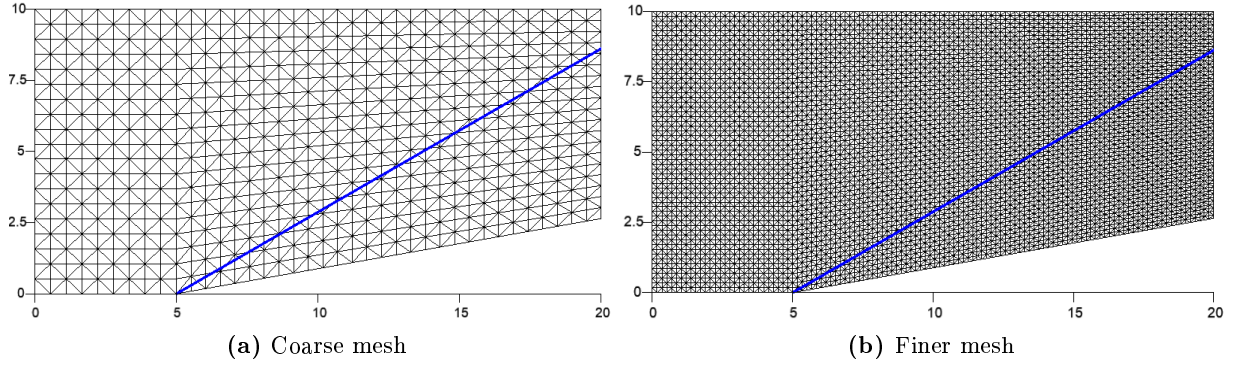


**Figure 2.3.2:** Oblique hydraulic jump - Uniform mesh used to test the convergence rate. The wavefront with  $\beta = 29.882$  deg is depicted by the blue line.

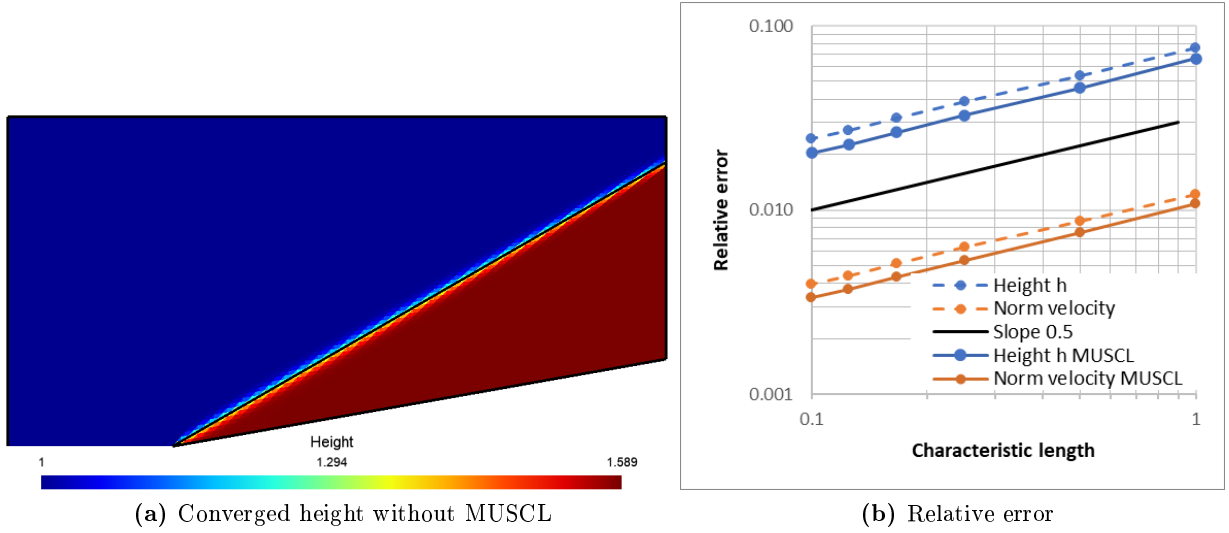


**Figure 2.3.3:** Oblique hydraulic jump - (left) Spatial distribution of the height  $h$ . The wavefront with  $\beta = 29.882$  deg is depicted by a black line. (right) Convergence rate of the height and norm of the velocity.

relative error  $\epsilon = \sqrt{\sum_i^N (h_i - h_{th})^2} / \sqrt{\sum_i^N h_{th}^2}$  can be calculated for both the height and the norm of the velocity. The characteristic length of the mesh is chosen equal to the length of the vertical sides of the triangles on the inflow boundary. By changing the number the number of elements along the inflow boundary, the number of cells along the horizontal direction is automatically adapted. The right part of Fig. 2.3.3 shows the convergence of the relative errors. The calculated convergence rate is close to 0.5 in the log-log space for both curves and for both with and without MUSCL.

At this point it is interesting to perform a first evaluation of the improvement brought by the second order reconstruction of the MUSCL method. Figure 2.3.4 shows the difference in height between computations run with and without the MUSCL scheme. One clearly see that the MUSCL method acts only in the area near the hydraulic jump, the rest of the domain remaining undisturbed. The curves of the height along a line parallel to the inclined bottom wall also show that the MUSCL method helps to better capture the hydraulic jump and that no additional spurious oscillations are introduced on both sides of the jump.

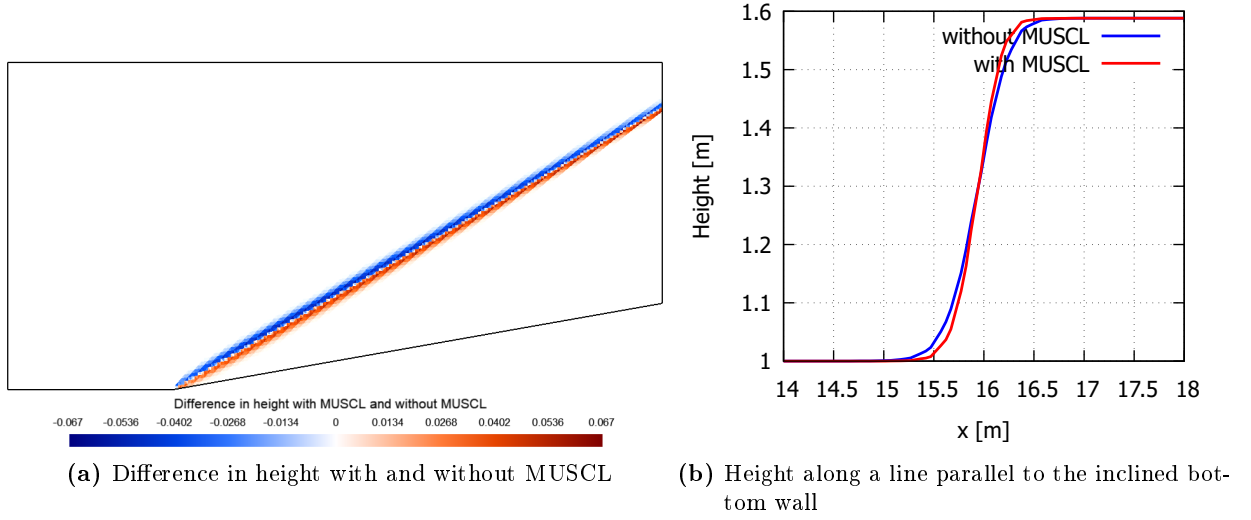


**Figure 2.3.4:** Oblique hydraulic jump - (left) Spatial distribution of the difference in height  $h$  with and without MUSCL. (right) Height along a line parallel to the inclined bottom wall with and without MUSCL.

## 2.4 Supercritical flow in symmetrical contraction

### 2.4.1 Bed slope and friction are neglected

Channel transitions should be designed to accomplish the necessary change in cross-section with as little flow disturbance as possible. In supercritical flows the standing waves produced by changes of direction in and downstream from the transition. In the present case the rectangular channel transition depicted in Fig. 2.4.1 has been chosen. The maximum flow disturbance results when the initial wave front intersection (point B) occurs at the downstream transition CC'. When the reflected waves BD and BD' intersect the channel walls below or above section CC', diamond-shaped cross waves develop in the channel. However, the change in wall alignment at section CC' results in negative wave disturbances that should tend to decrease the downstream effects of positive wave fronts. This should result in somewhat lower depths where the waves meet the downstream walls. The minimum disturbance occurs when the reflected waves BD and BD' meet the channel walls at section CC'. This, theoretically, results in the flow filaments again becoming parallel to the channel centerline. The surface disturbances are thus minimized when  $L = L_1 + L_2$ . If the reflected waves meet the walls upstream from section CC', the waves would be deflected again with a resulting increase in depth.

$$L_1 = \frac{b_1}{2 \tan \beta_1} \quad L_2 = \frac{b_3}{2 \tan(\beta_2 - \theta)} \quad (2.12)$$

Lai and Chan [14] chose the following parameters for the geometry: channel widths  $b_1 = 20m$  and  $b_3 = 10.548m$ , length of the contraction  $L = 22.233m$  for a wall deflection angle  $\theta = 12 \text{ deg}$ . The inflow Froude number is  $Fr_1 = 2.7$  and the inflow water level is  $h_1 = 1m$ . The wave angles calculated from relation 2.7 are  $\beta_1 = 33.6879 \text{ deg}$  and  $\beta_2 = 48.1022 \text{ deg}$ . The lengths given in Eq. (2.12) are  $L_1 = 15.0012m$  and  $L_2 = 7.2319m$ . In region 2, the water level is  $h_2 = 1.676m$ , the amplitude of the velocity is  $v_2 = 7.5726m/s$  and the Froude number is  $Fr_2 = 1.7875$ . In region 3, the water level is  $h_3 = 2.5618m$ , the amplitude of the velocity is  $v_3 = 6.2589m/s$  and the Froude number is  $Fr_3 = 1.2485$ .

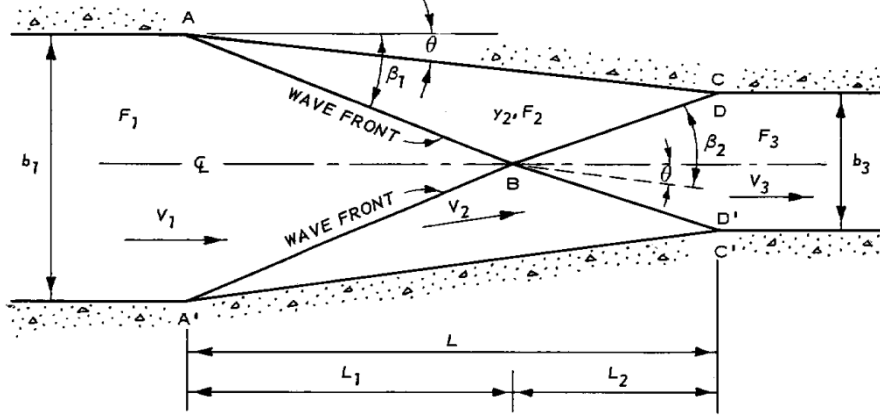


**Figure 2.4.1:** Supercritical flow in symmetrical contraction, picture from [13]

Two steady computations were run on different type of meshes, see the top part of Fig. 2.4.2. A first uniform mesh of nearly 30.000 cells and a second non-uniform mesh of nearly 20.000 cells. The second one has been designed on the basis of the knowledge of the theoretical values of  $\beta_1$ ,  $\beta_2$ ,  $L_1$  and  $L_2$ . Despite the higher number of cells, the uniform mesh fails at predicting the correct water level in region 3. Indeed the reflected wave front coming from the first intersection at  $L_1$  misses by little the exact location of  $L_2$ . This generates diamond-shaped cross waves in the channel downstream which reflects against the walls and intersects themselves. On the other side, despite having less cells, the non-uniform mesh predicts the correct value for  $L_2$  and no additional reflection is generated downstream. The correct theoretical water levels are computed in the three regions by the non-uniform mesh. No overshoot or oscillation are observed in the vicinity of the jumps; this indicates the validity and the robustness of the numerical method implemented in the present solver. The MUSCL scheme improves the results on the uniform mesh by reducing the amplitude of the diamond-shaped cross waves. On the contrary the MUSCL scheme does not impact significantly the results on the non-uniform mesh.

## 2.4.2 Bed slope and friction are taken into account

Other researchers studied the same flow topology with inclusion of the bed slope and the roughness (see e.g. Berger [15], Chaudhry [9] and Lee [16]). These studies are based on the experimental setup of Ippen [17]. The dimensions of the channel were  $b_1 = 2ft$ ,  $b_3 = 1ft$  and  $L = 4.78ft$  (angle  $\theta = 6deg$ ). The inflow conditions are  $Fr_1 = 4$ , and  $h_1 = 0.1ft$ . The bed slope is  $S_0 = 0.05664$  and the Manning coefficient of roughness  $n = 0.0107m^{1/3}/s$ .

A non-uniform mesh has been built on the basis of a first solution computed on an uniform mesh. The extraction of the gradient in water level allowed the generation of refined areas thanks to the mesh generator Gmsh [18]. An example of such a mesh is shown on the top part of Fig. 2.4.3. By neglecting the bed slope and the friction, the theoretical values for  $\beta_1$ ,  $\beta_2$ ,  $L_1$  and  $L_2$  were computed:

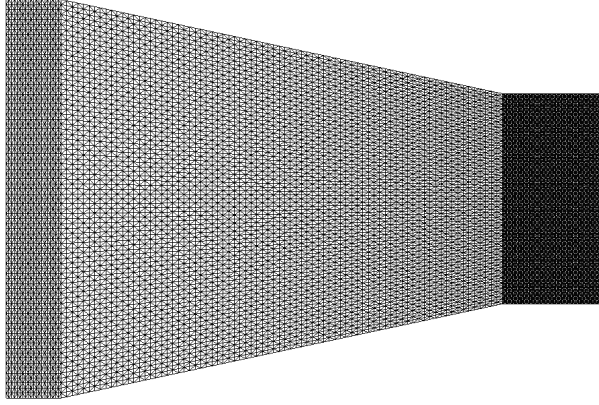
$$\beta_1 = 19.68deg \quad \beta_2 = 23.59deg \quad (2.13)$$

$$L_1 = 0.8523m \quad L_2 = 0.4808m \quad (2.14)$$

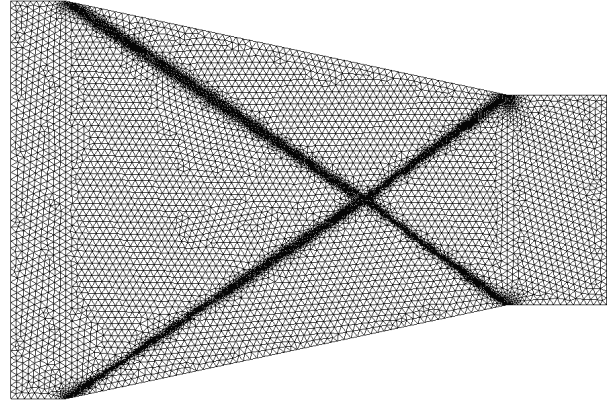
$$h_2 = 0.147ft \quad h_3 = 0.2024ft \quad (2.15)$$

$$Fr_2 = 3.178 \quad Fr_3 = 2.703 \quad (2.16)$$

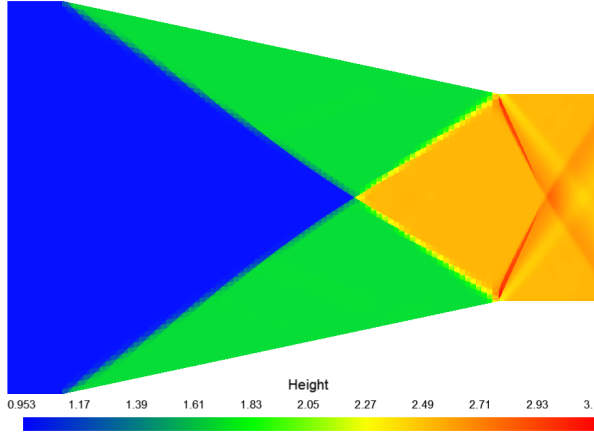
These values were naively depicted on Fig. 2.4.3. One observes two things:



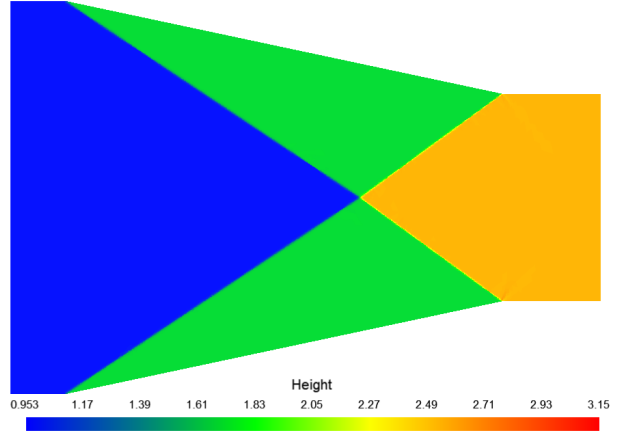
(a) Uniform mesh



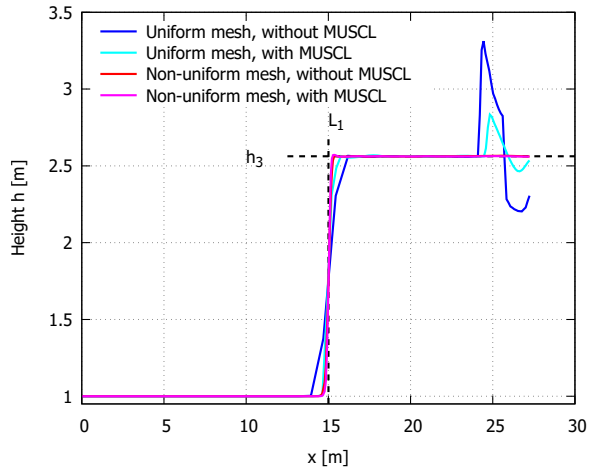
(b) Non-uniform mesh



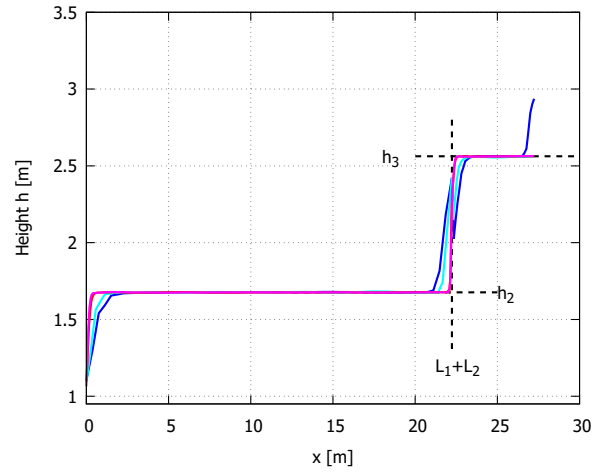
(c) Water level with uniform mesh, MUSCL scheme



(d) Water level with non-uniform mesh, MUSCL scheme



(e) Water level along the centerline



(f) Water level along the wall

**Figure 2.4.2:** Supercritical flow in symmetrical contraction - [top] Meshes used for the two computations and [middle and bottom] their respective water levels.

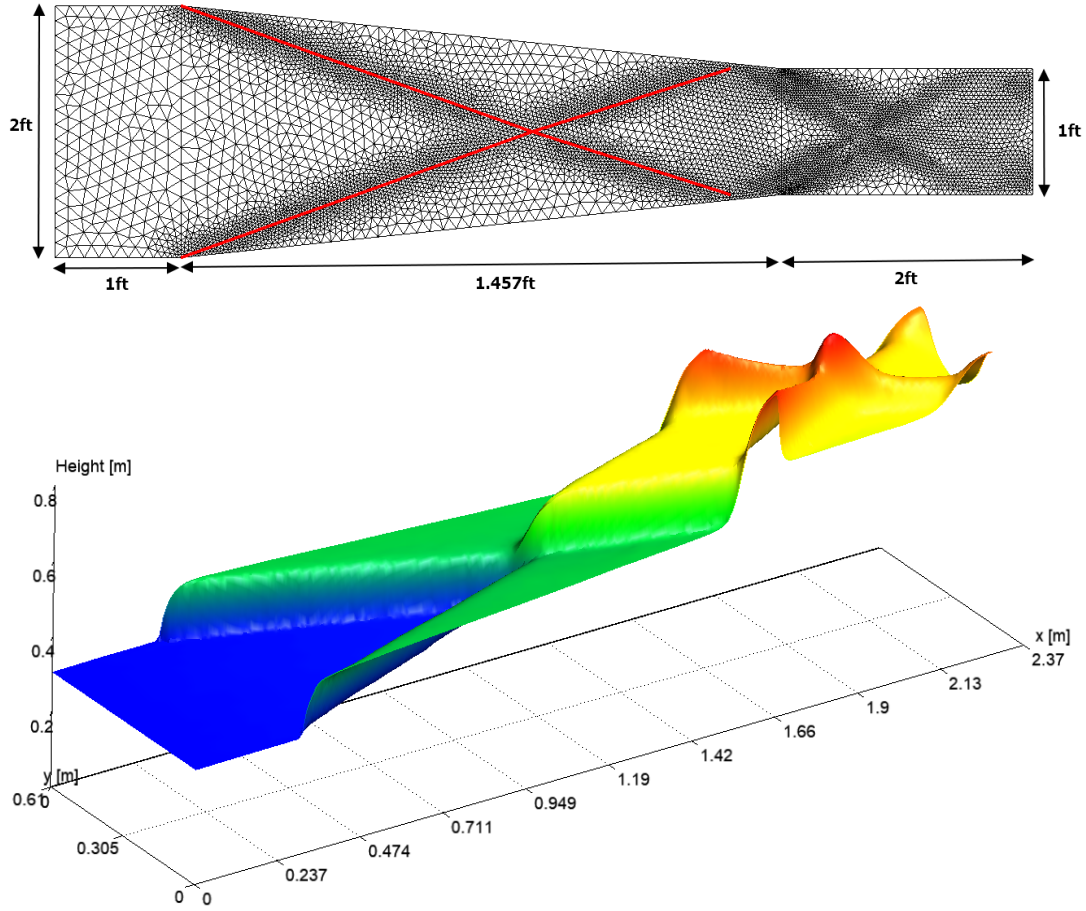


**Figure 2.4.3:** Supercritical flow in symmetrical contraction including bed slope and friction - [top] Geometry and mesh generated by Gmsh [18] and [bottom] water level for  $S_0 = 0.05664$  and  $n = 0.0107$ .

- The effect of the bed slope and friction taken into account during the generation of the mesh shifts the first intersection between the wave fronts upstream in comparison with the theory (red curves).
- The intersection of the reflected waves with the walls occurs upstream of section of section CC' (Fig. 2.4.1) where the converging channel reverts to parallel walls. Diamond-shaped cross waves will thus be generated downstream of section CC'.

The bottom part of Fig. 2.4.3 shows the water level of the computation that includes the geometrical and friction slopes. One clearly see the generation of the oblique shock waves on each side of the contraction, their interaction and their reflection on the walls. One also clearly sees the generation of the diamond-shaped cross waves downstream of CC' as explained above. Because no free-access is granted to the work of Ippen [17], it can not be checked whether this last effect was desired or not. However all the succeeding studies (Berger [15], Chaudhry [9] and Lee [16]) also put forward the generation of diamond-shaped cross waves in region 3.

The variation in height along the centerline and along the lateral walls is shown in Fig. 2.4.4. The height has been made non-dimensional by the height  $h_1$  at the entry of the channel. Both computations (with and without bed slope and friction) provide similar shapes in comparison with the numerical results from Chaudhry [9]. The locations of the jumps are similar and one clearly see the constant level of the height in the area away from the jumps, in the case where

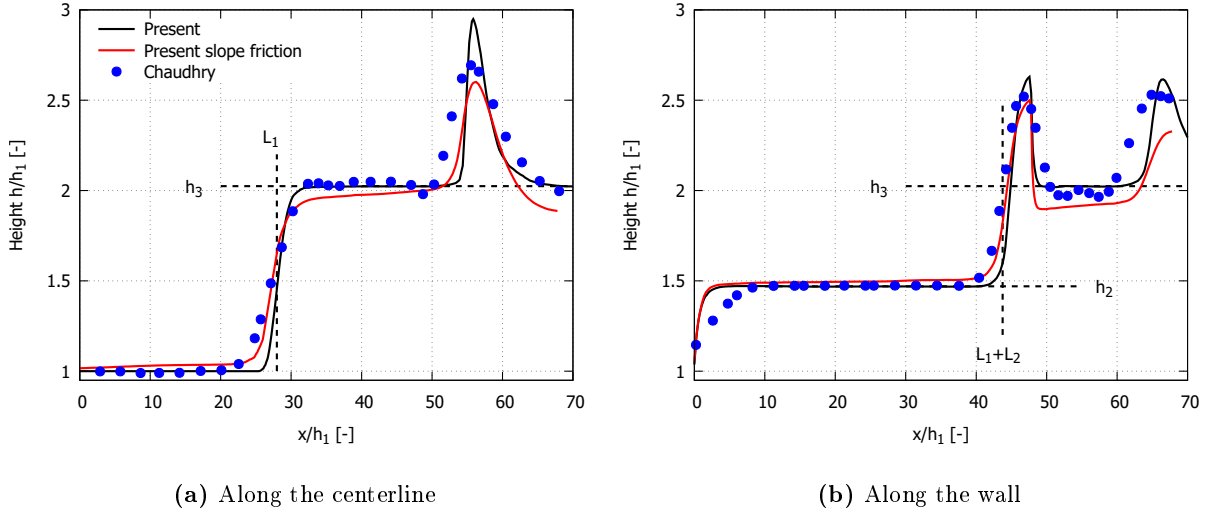


**Figure 2.4.4:** Supercritical flow in symmetrical contraction including bed slope and friction - Water level along the centerline and along the wall. The numerical results from Chaudhry [9] are put for comparison. The geometrical/friction slopes ( $S_0 = 0.05664$  and  $n = 0.0107$ ) are included in the red curves but not in the black ones.

the slopes are neglected. If both slopes are taken into account, then a slight increase in height takes place as the water moves downstream. The addition of the roughness dampens the peaks where the walls are parallel again. A very good agreement is met with the theoretical values for the computation without bed slope or friction.

The behaviour of the water surface in this supercritical flow scenario is quite sensitive to bottom friction. Figures 2.4.5 and 2.4.6 show the water surface level using several values of the Manning coefficient ( $n = 0.011, 0.013$  and  $0.015$ ) at constant bed slope  $S_0 = 0.05664$ . Theoretical results from the Bresse's extension of Eq. (2.3) to nonprismatic geometries of the 1D momentum equation (see Eq. (2.17)) are also given for comparison. The 2D shallow water theory predicts a complex pattern of oblique standing waves, while the 1D theory yields gradually varied supercritical flow throughout. Qualitatively, both the 1D and 2D models capture the overall water surface profile along the centerline and along the wall. An increase in the friction coefficient leads to an increase of the initial wave angle ( $\beta \approx 20.3^\circ$  for  $n = 0.011$ ,  $\beta \approx 21.2^\circ$  for  $n = 0.013$  and  $\beta \approx 22.5^\circ$  for  $n = 0.015$ ). This implies that, at high friction coefficients, the hydraulic jump hits the wall for the first time more upstream than at small friction coefficients. As a result the peaks in water level downstream of the contraction are broader for large  $n$  and show more reflections than for small  $n$ .

The behaviour of the water surface in this supercritical flow scenario is quite sensitive to bed slope. Figures 2.4.7 and 2.4.8 show the water surface level using several values of the bed slope ( $n = 0.011, 0.013$  and  $0.015$ ) at constant Manning friction coefficient  $n = 0.011$ . An increase in the friction coefficient leads to a decrease of the initial wave angle ( $\beta \approx 22^\circ$  for  $S_0 = 0.01$ ,  $\beta \approx 20.3^\circ$  for  $S_0 = 0.05664$  and  $\beta \approx 19.1^\circ$  for  $S_0 = 0.09$ ). As a consequence the frequency of the peaks along the centerline and along the wall is higher at small bed slopes than at big bed slopes. At  $S_0 = 0.09$  the peaks in water height are rapidly damped and the second reflection on the centerline is of reduced amplitude. This is because the first reflection on the wall is located near the throat of the contraction and is thus strongly damped by the negative wave front. At  $S_0 = 0.01$  the Froude number tends to stabilize around 1.7 whereas at  $S_0 = 0.09$  the supercritical nature of the flow is more evident.

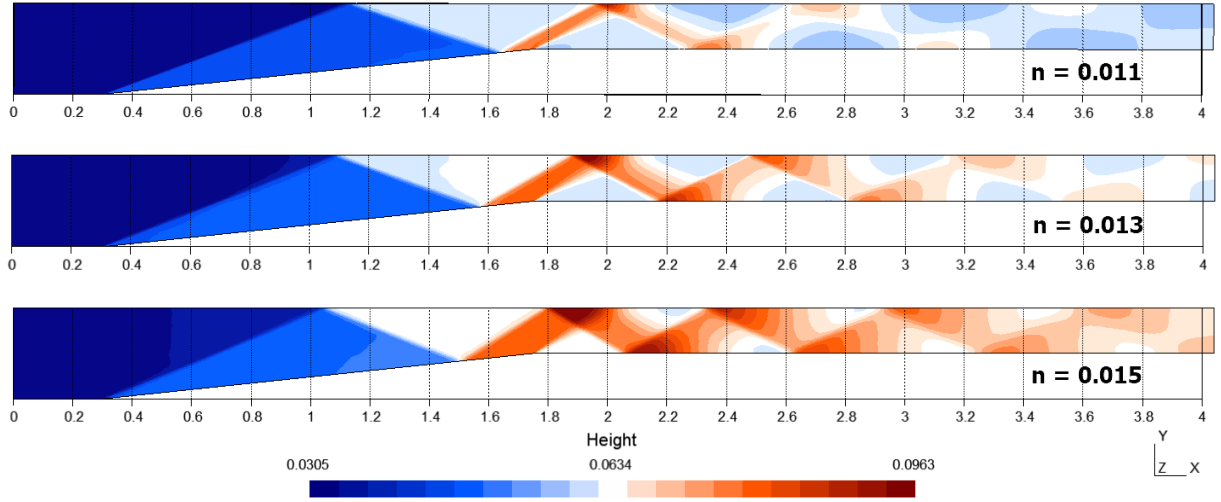


**Figure 2.4.5:** Supercritical flow in symmetrical contraction including bed slope and friction - Influence on the solution of the friction coefficient for constant bed slope ( $S_0 = 0.05664$ ). From top to bottom  $n = 0.011$ ,  $0.013$  and  $0.015$ .

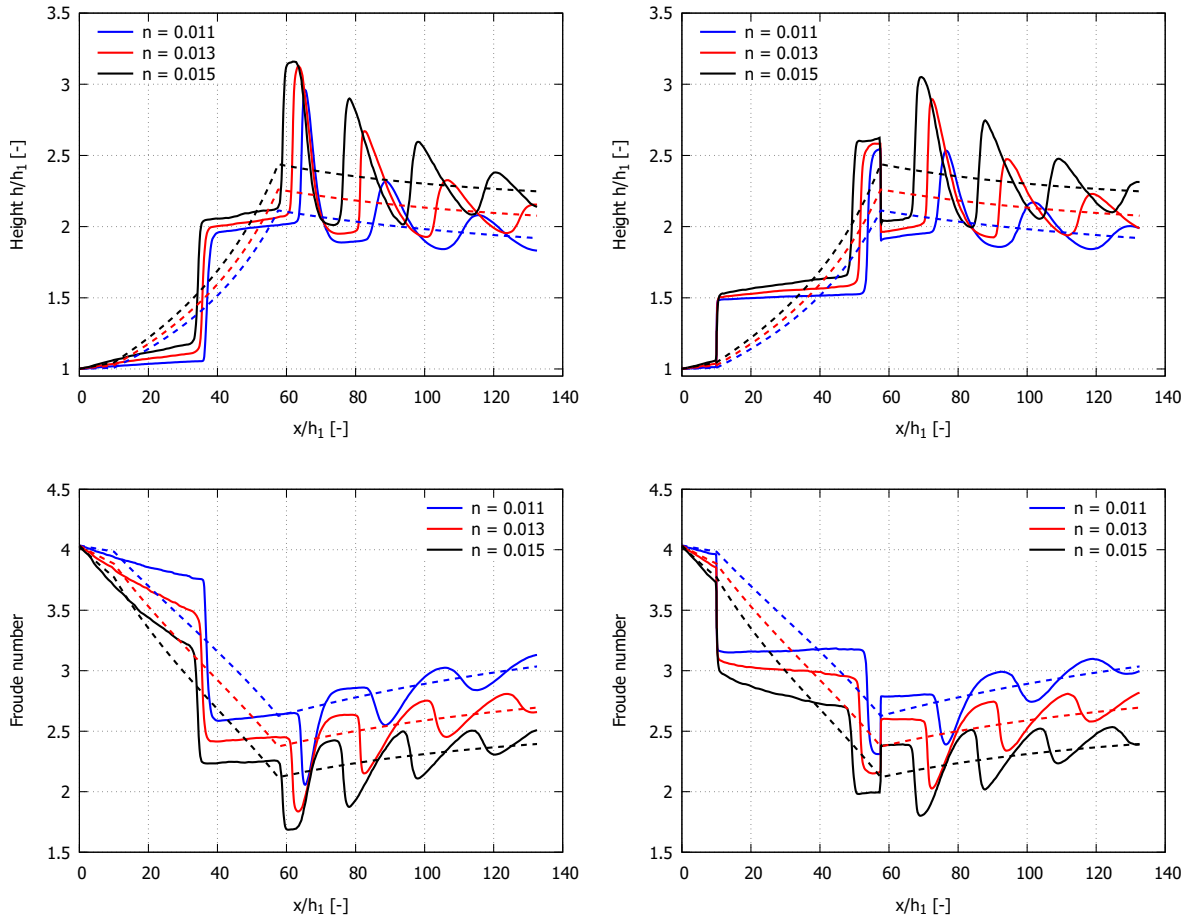


**Figure 2.4.6:** Supercritical flow in symmetrical contraction including bed slope and friction - Influence on the solution of the friction coefficient for constant bed slope ( $S_0 = 0.05664$ ). (left) Along the centerline and (right) along the wall. (top) Water level  $h$  and (bottom) Froude number. (full lines) 2D shallow water model and (dashed lines) Bresse's extension of Eq. (2.3) to nonprismatic geometries of the 1D momentum equation (Eq. (2.17)).



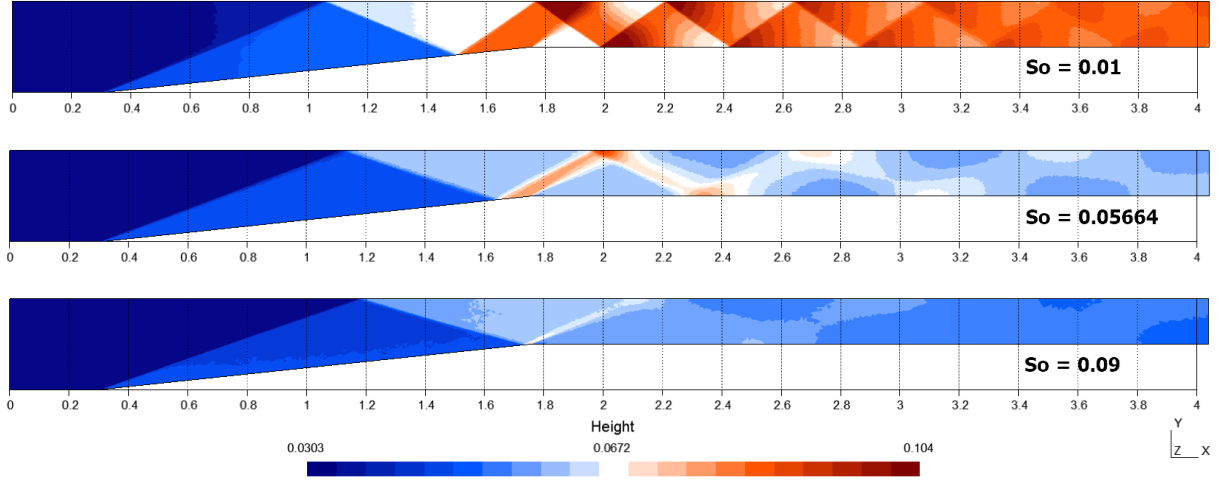


**Figure 2.4.7:** Supercritical flow in symmetrical contraction including bed slope and friction - Influence on the solution of the friction coefficient for constant Manning friction coefficient ( $n = 0.011$ ). From top to bottom  $S_0 = 0.01$ ,  $0.05664$  and  $0.09$ .

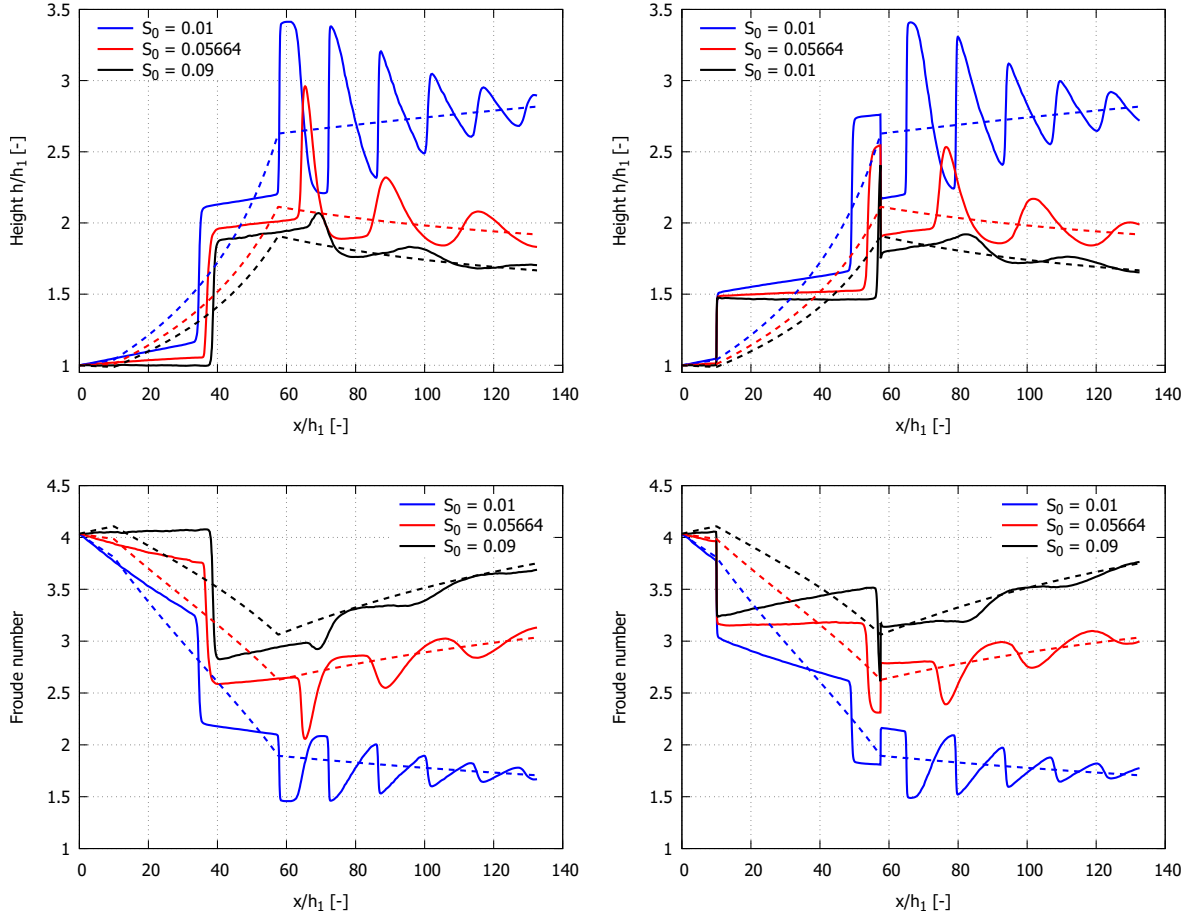


**Figure 2.4.8:** Supercritical flow in symmetrical contraction including bed slope and friction - Influence on the solution of the friction coefficient for constant Manning friction coefficient ( $n = 0.011$ ). (left) Along the centerline and (right) along the wall. (top) Water level  $h$  and (bottom) Froude number. (full lines) 2D shallow water model and (dashed lines) Bresse's extension of Eq. (2.3) to nonprismatic geometries of the 1D momentum equation (Eq. (2.17)).

### 2.4.3 Irregular shock reflection

The previous two configurations showed regular shock reflections (RR) at the wall and on the channel axis. This corresponds to configurations (a) and (b) on Fig. 2.4.9 and appears at high Froude numbers and low deflection angles  $\theta$ .

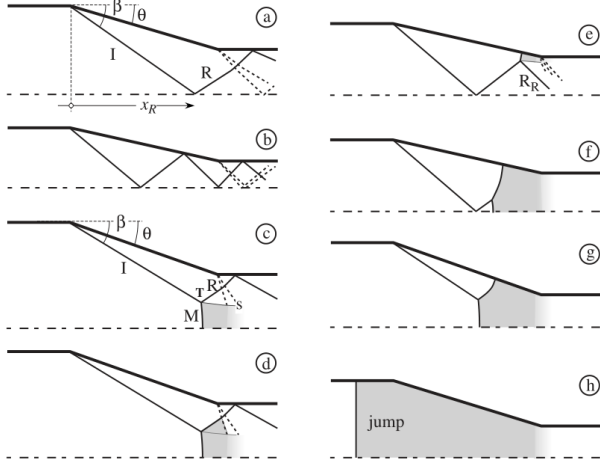


**Figure 2.4.9:** Irregular shock reflection - Different shock wave patterns in a linear channel contraction. Solid lines denote shock wave fronts, dashed lines denote the fan originating at the downstream edge of the contraction; shaded area denotes subcritical flow. I and R are the incident and reflected shock, M is the Mach stem. Figure from Defina [19].

one has two strong IRs off the converging wall and the channel axis and two facing pockets of subcritical flow across the throat. At  $Fr = 4.10$  the subcritical regions increase in size and finally merge forming one single stable band of subcritical flow all across the throat. Only one IR is present near the converging wall, the shock pattern near the channel axis does not have a reflected shock. Lowering further the Froude number triggers an unstable transition to flow configuration with a 2D jump in the contraction or a normal jump upstream of the contraction (case (h)). The shapes of the results is very similar to those in Defina [19].

A second category of shock reflection is the irregular one (IR). This corresponds to configurations (c) and (d) on Fig. 2.4.9 in the case of an IR off the channel axis and to configuration e for an IR off the converging wall. The IR can be either weak or strong and shows three shock waves (incident I, reflected R and Mach stem M) meeting at the triple point T. A contact discontinuity, the slip stream s, also originates at the triple point, and separates the flow behind the reflected shock from the flow behind the Mach stem. Across the slip stream water depth is continuous while flow velocity (hence, the Froude number) is discontinuous.

Because of the obvious symmetry of the flow, only one half of the channel is meshed and computed. Let's take the same geometry as Defina [19] with the ratio of channel widths  $b_3/b_1 = 0.3$  and the deflection angle  $\theta = 15^\circ$ . The channel has a flat bottom (bed slope  $S_0 = 0$ ) and the flow is inviscid (no friction). On Fig. 2.4.10, the Froude number at the inlet is decreased from  $Fr = 4.20$  to  $Fr = 4.10$ . In this configuration, one gets the configuration e on Fig. 2.4.9. Until  $Fr = 4.15$ ,

## 2.5 Transcritical flow in long channels

Let us consider a transcritical flow past a mild contraction in a long channel. The channel geometry is depicted in Fig. 2.5.1: a long channel with a width  $b_1$  shows a symmetric contraction characterized by the length and width of the narrowest section  $b_2$  and  $L_b$  respectively and by the length of the symmetric contracting/expanding sections  $L_e$ . The distance between the upstream inlet boundary to the contraction is  $L_u$ , the steady flow discharge is  $Q$  and the channel bed slope is  $S_0$ .

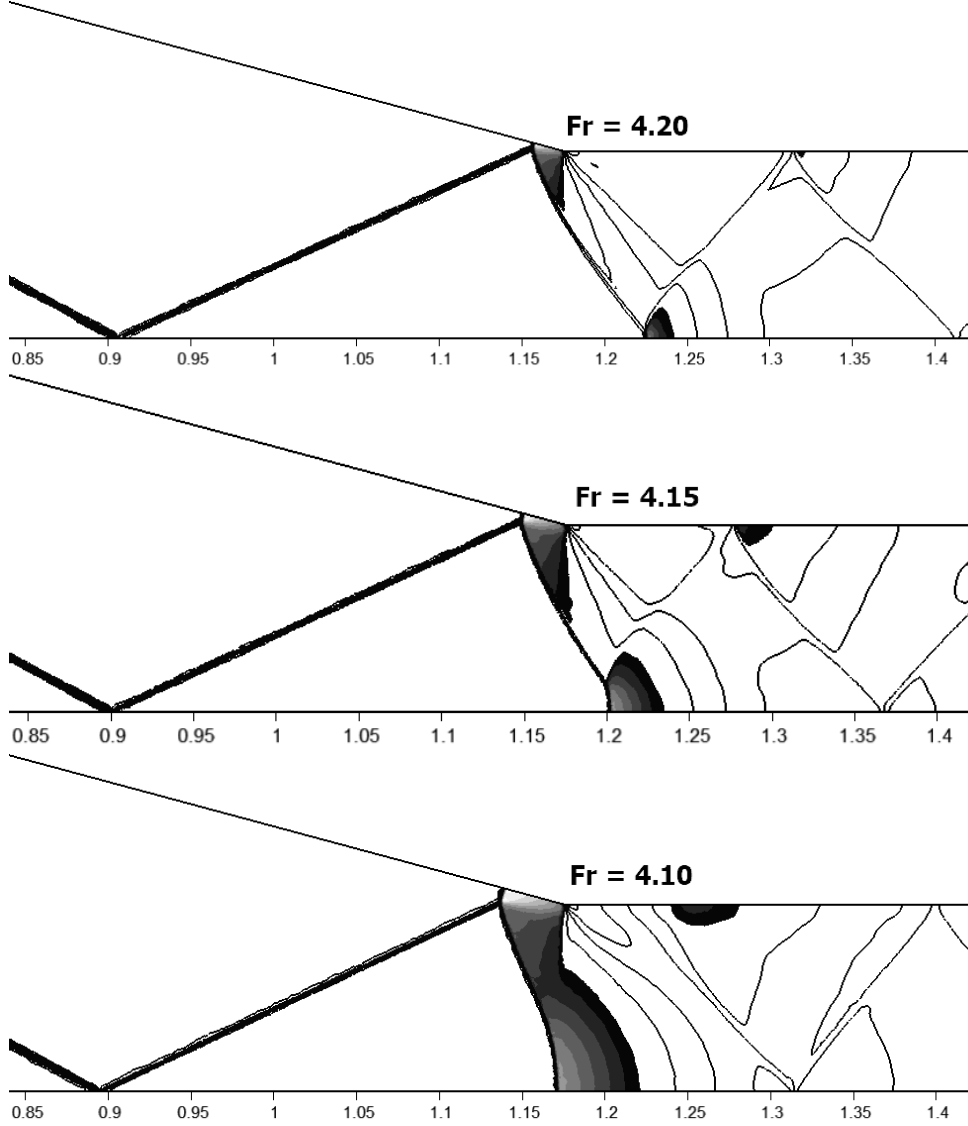


**Figure 2.4.10:** Steady configuration with an IR off the converging wall ( $\theta = 15$  deg and  $b/B = 0.3$ ): from top to bottom  $Fr = 4.20$ ,  $Fr = 4.15$  and  $Fr = 4.10$ .  $Fr = 4.15$  has two strong IRs off the converging wall and the channel axis and two facing pockets of subcritical flow across the throat.  $Fr = 4.10$  has one stable band of subcritical flow all across the throat. Isolines of Froude number and highlight of the subcritical areas.

### 2.5.1 Theoretical 1D model

Assuming uniform velocity across the channel width, hydrostatic pressure and steady-state flow conditions, we model gradually varied flow in channels of constant slope and discharge  $Q$ , using Bresse's extension of Eq. (2.3) to nonprismatic geometries of the 1D momentum equation

$$\frac{dh}{dx} = \frac{S_0 - S_f + \frac{Q^2}{gA^3} \frac{\partial A}{\partial x}}{1 - \frac{Q^2 b}{gA^3}} \quad (2.17)$$

$$S_f = \left( \frac{nV}{R^{2/3}} \right)^2 = \left( \frac{nQ(b + 2h)^{2/3}}{(bh)^{5/3}} \right)^2$$

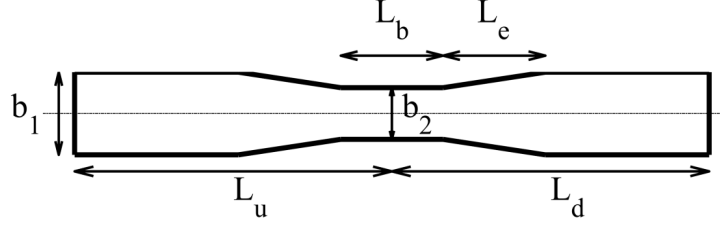


**Figure 2.5.1:** Transcritical flow in long channels - Geometry of the flow.

Herein  $x$  is the distance along the bottom of the channel and  $b$  is the local top channel width. Rectangular cross-sections are used in the present case so that  $A = bh$  and the partial derivative  $\partial A / \partial x = h \partial b / \partial x$ .

The channel operates under mild slope conditions: the overall hydraulic control is exerted from downstream to upstream sections and undisturbed flow is subcritical. Geometrically, we consider long channels where the total discharge is known, and with free overfall conditions at the outlet. For hydraulically long channels, where the contraction is sufficiently far from the outlet, the water surface reaches the contraction with uniform depth,  $y_n$ . For finite, hydraulically short channels, the specific energy and depth at the downstream end of the contraction (point A in Fig. 2.5.2) are determined by upstream integration of Eq. (2.17), with initial condition  $h = y_c$  at the outlet of the channel. The resulting backwater curve approaches  $y_n$  asymptotically from the critical depth — it is a M2 profile.

To reconstruct the water profile in transcritical scenarios, we begin by identifying the control section inside the channel contraction; that is, the upstream-most section where critical depth is observed. In the present case, the control section corresponds to the downstream edge of the narrowest segment of the contraction (point A in Fig. 2.5.2). Hydraulic control dictates that we must integrate Eq. (2.17) forward, with initial condition  $h = y_c$ , ending at a hydraulic jump to the approaching M2 profile. We distinguish between the case in which the jump remains in the expansion zone (top of Fig. 2.5.2), and the lower-energy case in which the jump is expelled out of the channel constriction (bottom of Fig. 2.5.2). In either case the location of the hydraulic jump is identified as the intersection between the specific momentum functions of the M3 and M2 curves. The physical length and complex internal structure of the jump are neglected, so for a rectangular channel the location is at the unique point where the depth of the approaching M2 profile equals the conjugate of the upstream depth,  $h_{u,conj}$ . We use the hydraulic jump formula for rectangular channels:

$$h_{u,conj} = \frac{h_u}{2} \left( \sqrt{1 + 8Fr_u^2} - 1 \right) \quad (2.18)$$

where  $Fr_u$  is the Froude number computed with the upstream depth  $h_u$ . Upstream from the critical section the hydraulic control reverts to being exercised from downstream sections. Hence, the water profile is constructed through backwards integration of Eq. (2.17), with initial condition  $h = y_c$  at point A. Upstream from the initial edge of the constriction we may observe either M1 or M2 profiles, depending on whether the normal depth is asymptotically approached from above or from below.

## 2.5.2 Results

To test a realistic outlet boundary condition, we compare the 1D and 2D model predictions for a mild contraction,  $b_1 = 40m$ ,  $b_2 = 26.5m$ , same length of the converging/expanding sections,  $L_e = 20m$ , discharge  $Q = 500m^3/s$ , the channel bed slope is  $S_0 = 0.002$ . The Manning friction coefficient is  $n = 0.04$  for the 2D computations and is  $n = 0.0389$  for the 1D computa-

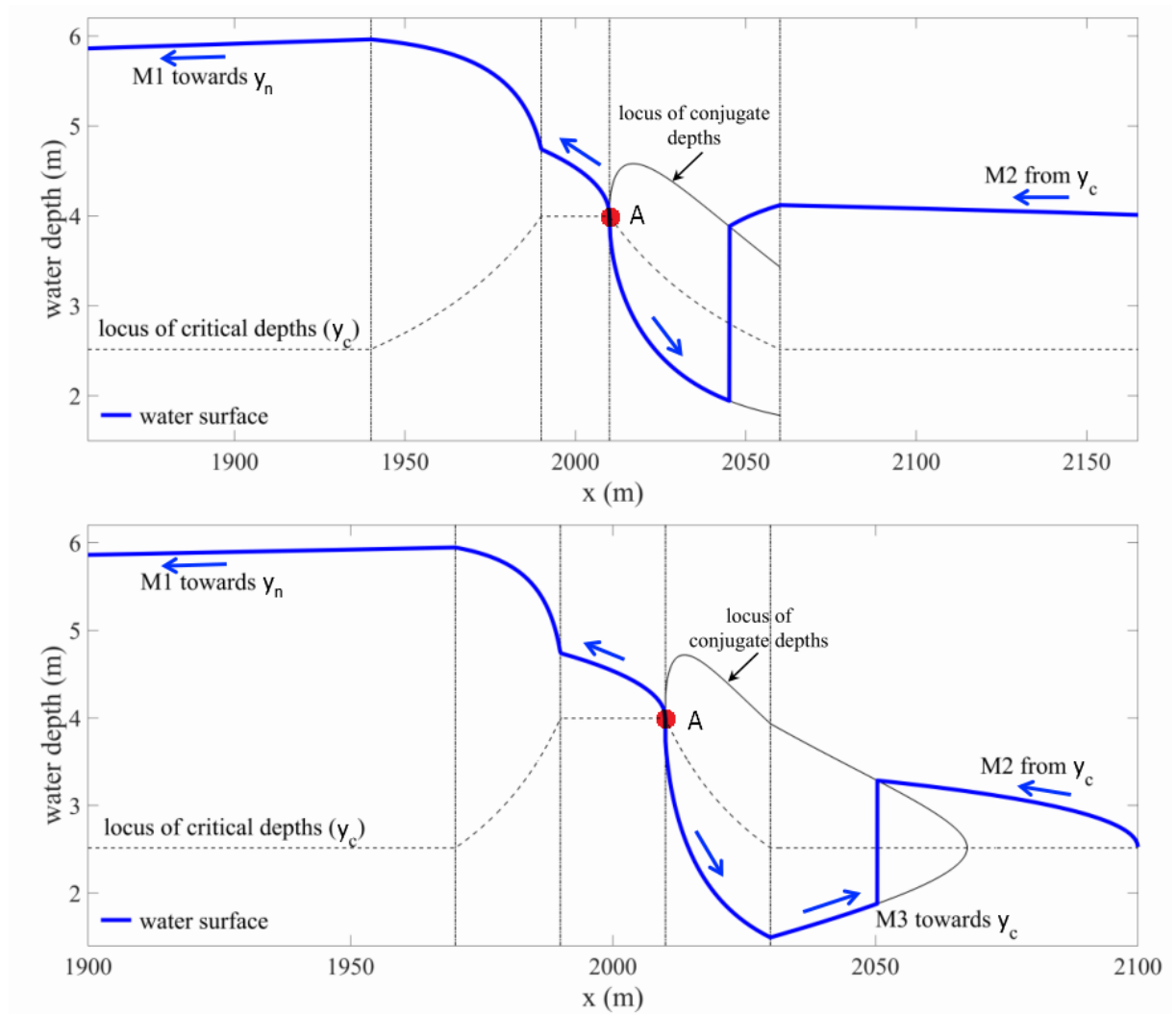


**Figure 2.5.2:** Transcritical flow in long channels - Construction of water surface profiles through the direction of integration of Eqs. (2.17). Figure from Cueto-Felgueroso [10]. (Top) Sample case where the hydraulic jump is contained within the expansion zone and (bottom) a sample case where the hydraulic jump is expelled outside of the expansion zone.

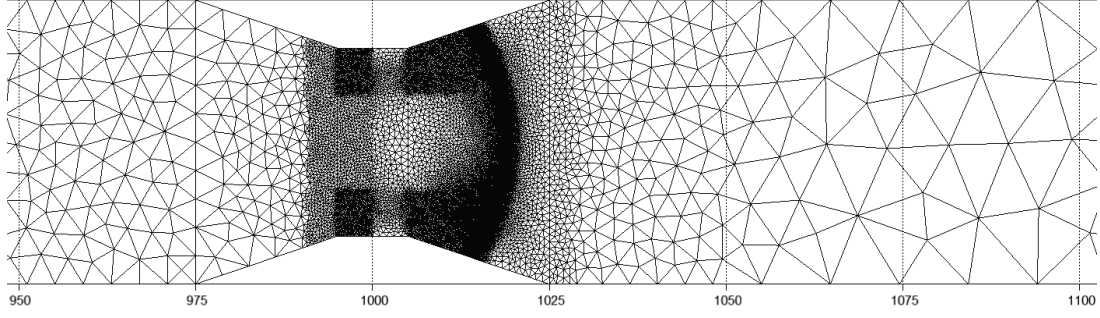


**Figure 2.5.3:** Transcritical flow in long channels - Mesh created after a first computation that located the hydraulic jump for  $L_d = 250m$ .

tions. Subcritical boundary conditions are imposed at the inlet ( $h_{inlet} = y_n = 4.543m$ ,  $u_{inlet} = Q/b_1 h_{inlet} = 2.751m/s$ ) and critical boundary conditions at the outlet ( $h_{outlet} = y_c = 2.516m$ ). Several values of the distance to the outlet,  $L_d$ , where we imposed free overfall conditions. For this long channel, friction losses are large enough so that the available specific energy at the contraction is controlled by a backwater curve starting from the critical depth at the outlet. We induce the onset of transcritical flow at the throat section by reducing the distance to the outlet,  $L_d$ , from  $4000m$  to  $75m$  (see Figs. 2.5.4 and 2.5.5).

Extra care was taken during the generation of the 2D mesh. Indeed, as shown in Fig. 2.4.2, the capture of the hydraulic jump is crucial in the precision of the downstream section. Thus an initial computation allowed to detect the location of the hydraulic jump. A second mesh has then been built for each  $L_d$  with a refinement around the hydraulic jump (see Fig. 2.5.3 for the mesh for  $L_d = 250m$ ). Both triangular and rectangular meshes were built for each value of  $L_d$  and their respective results were compared.

The 1D model predicts transcritical flow conditions for all the values of  $L_d$ . The 2D model predicts transcritical flow conditions for the smallest values of  $L_d$  whereas  $L_d = 500m$  and  $L_d = 4000m$  are near-critical (see Figs. 2.5.4 and 2.5.5). The hydraulically short channels ( $L_d \leq 250m$ ) exhibit repelled hydraulic jumps that join at the middle of the section. The 1D computation for  $L_d = 500m$  predicts a jump. On the opposite the 2D computation shows that the repelled hydraulic jumps do not meet at the middle of the section but remain near the side walls. This behaviour is similar to the theoretical curve for  $L_d = 4000m$  where the height reaches the critical depth  $y_c$  at point A and then follows the M1 towards the uniform depth  $y_n$ . The location of the hydraulic jump and the M1-M2 curves are very similar between the 1D and 2D models. However a discrepancy exists between these models inside the contraction for the gradually varied water surface profile leading to the toe of the jump. Indeed large Froude number conditions lead to flow patterns dominated by oblique shocks that render the 1D analysis invalid in the expansion zone. The discrepancy is the highest for  $L_d = 75m$  where the hydraulic jump has been expelled outside of the expansion zone. The 1D model predicts a M3 that goes up towards  $h = y_c$  but the 2D model predicts a toe of the jump that continues its descent. The 2D models based on the triangular and rectangular meshes show very similar results. The most visible difference is for  $L_d = 500m$  near  $Fr = 1$ .

## 2.6 Partial breach of a dam

This test case analyses an unsteady flow resulting from a partial dam break or the instantaneous opening of sluice gates. The breach is nonsymmetrical to demonstrate analysis of a general case. The bathymetric term is not considered in this case (constant elevation of the ground). This unsteady flow does not have any analytical solution but it has been reported by Fennema

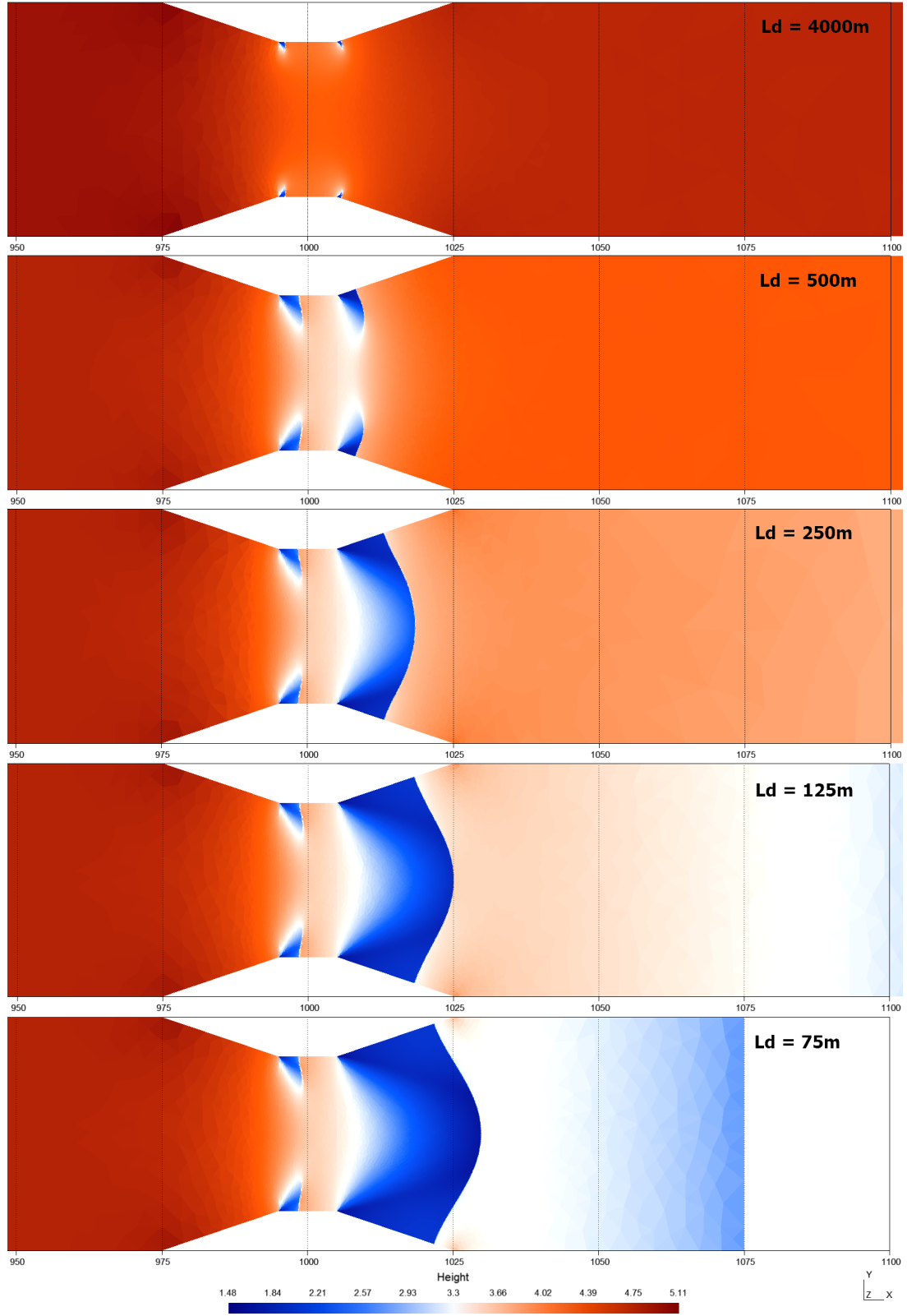


**Figure 2.5.4:** Transcritical flow in long channels - Onset of transcritical flow in the 2D model by reducing the distance to the outlet  $L_d$  from (top) 4000m to (bottom) 75m.

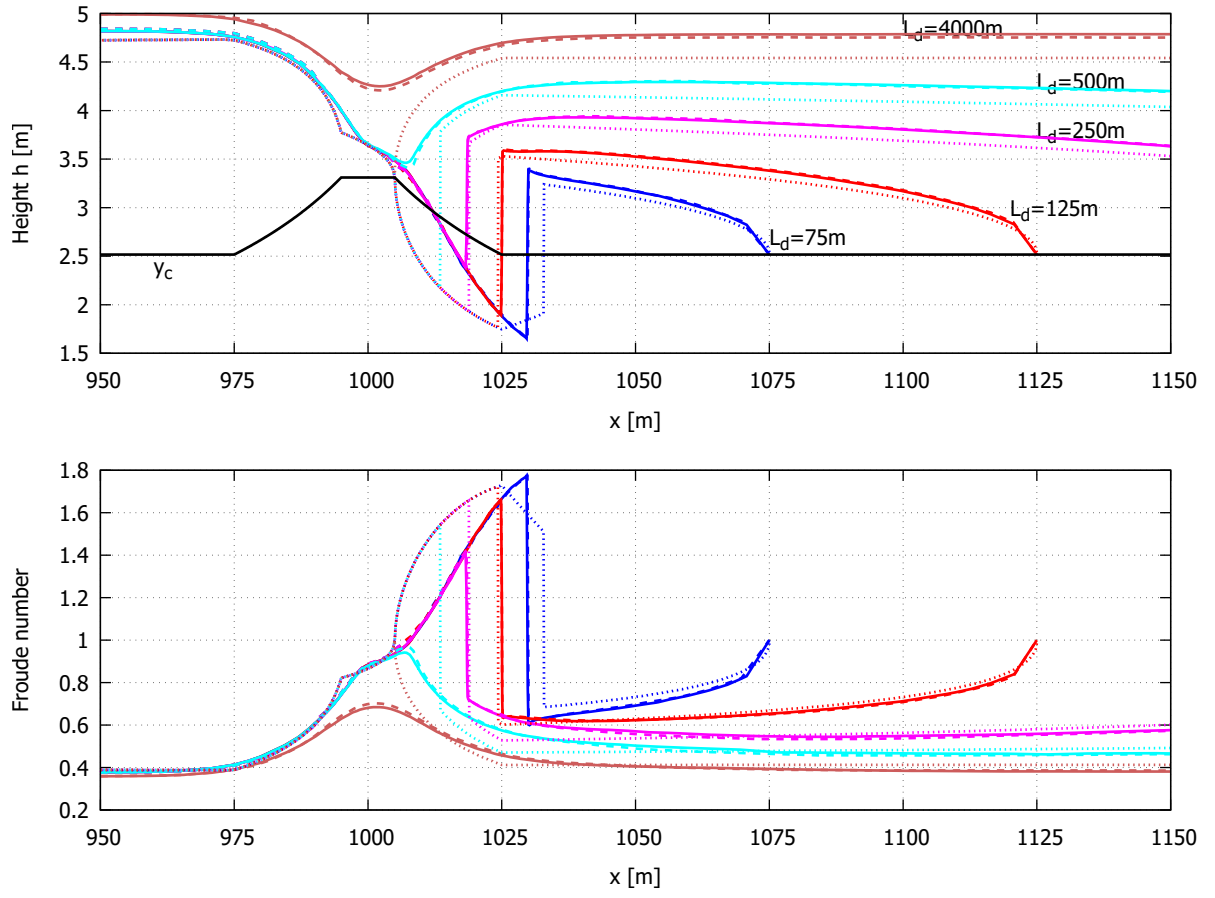


**Figure 2.5.5:** Transcritical flow in long channels - Onset of transcritical flow in the 1D (dotted lines) and 2D models based on a triangular mesh (full lines) or on a rectangular mesh (dashed lines) by reducing the distance to the outlet  $L_d$ . (top) Height and (bottom) Froude number.



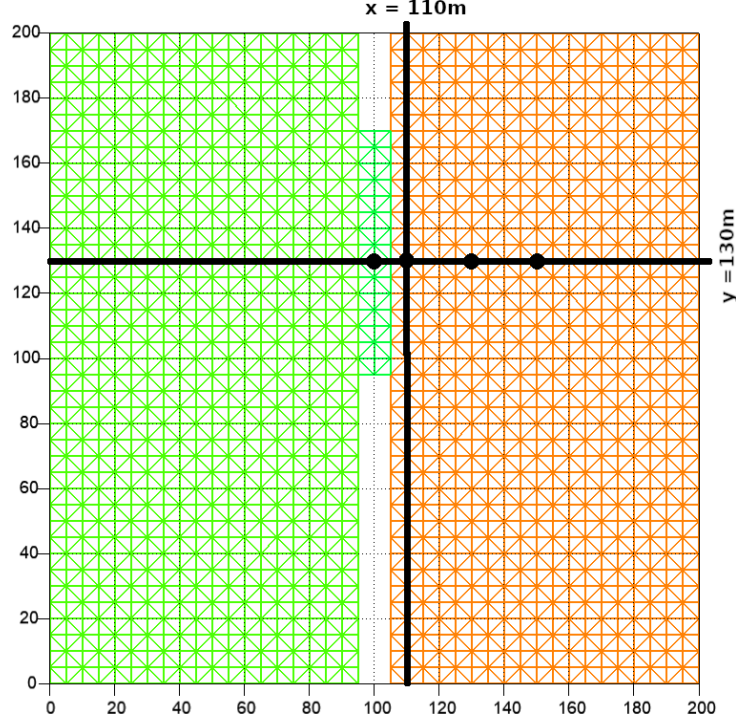


**Figure 2.6.1:** Partial dam breach - Geometry and mesh.

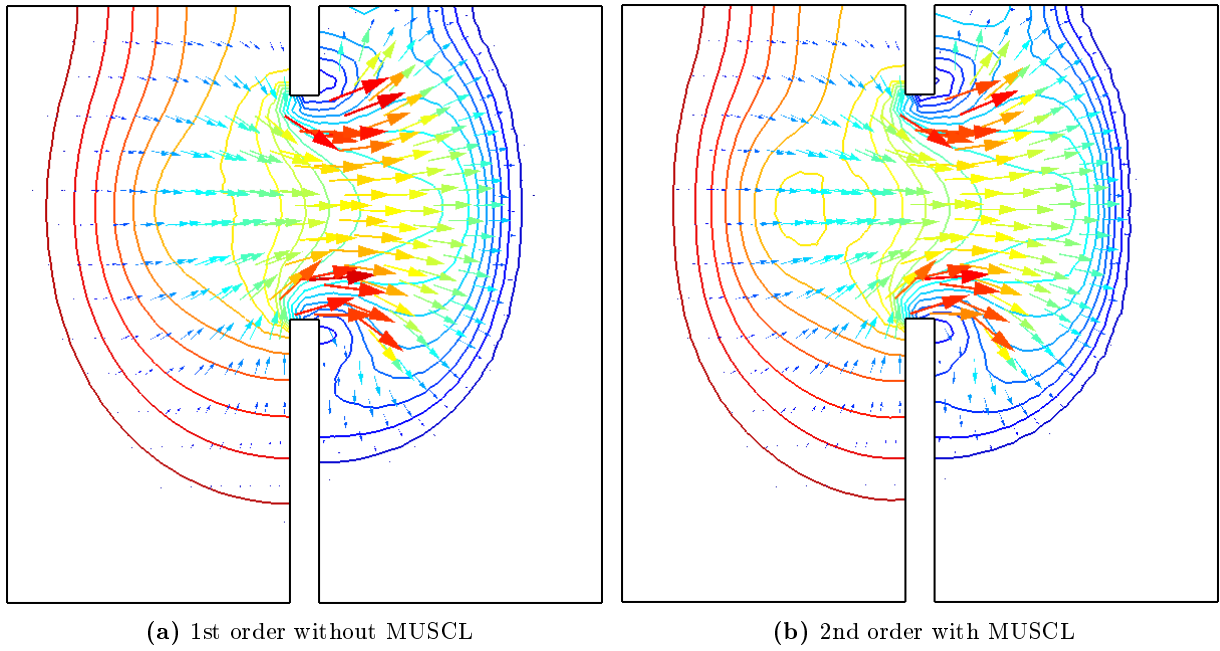
and Chaudhry [20], Bermúdez *et al.* [5], Valiani *et al.* [12], Chaudhry [9] and Biscarini *et al.* [21].

The computational domain is depicted in Fig. 2.6.1. It contains a  $200m \times 200m$  closed domain (only non-slip walls are present), the breach is  $75m$  wide and the structure of the dam is  $10m$  thick in the direction of the flow. The mesh is built from  $5m \times 5m$  isosceles right triangles. The initial conditions are still water with a height of  $10m$  in the left half and  $5m$  in the right half (including the portion that models the dam/sluice gate).

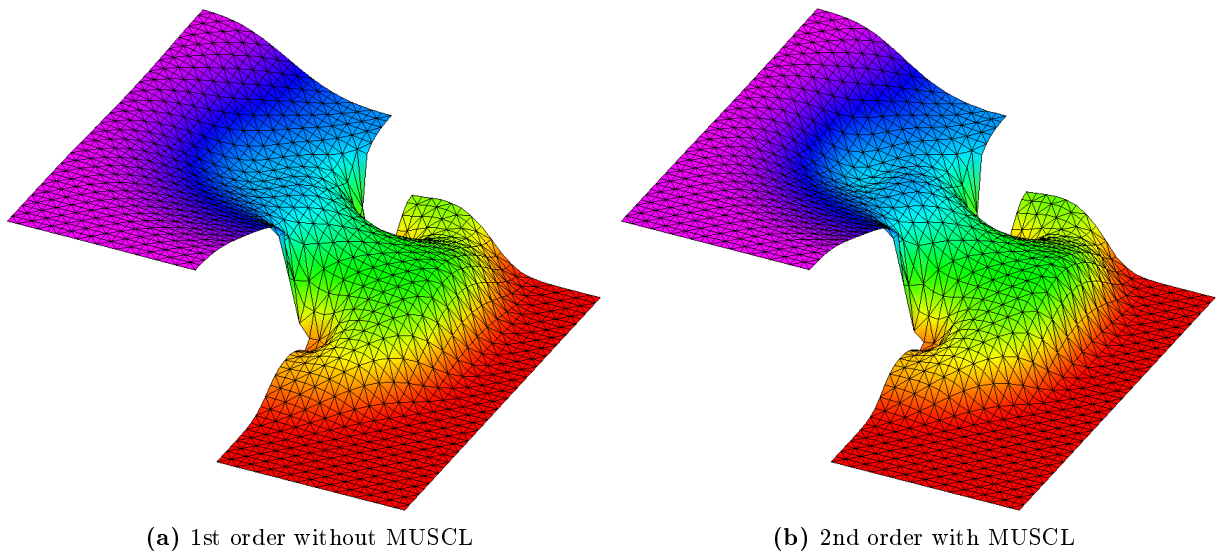
The duration of the computation is  $t = 7.2s$ . At this time, the bore is well developed in the central portion and the wavefront has reached one bank of the channel. Figure 2.6.3 shows the three-dimensional water surface at the final time and Figure 2.6.2 shows iso-value lines of the water height and velocity arrays. In the computation run with the MUSCL method, a region of peak/valley appears on the left side of the dam. This phenomenon is also observed in Fennema and Chaudhry [20] and Biscarini *et al.* [21]. Moreover the iso-value lines are more condensed on the right side for the MUSCL method. This denotes a better capture of the wavefront when the MUSCL scheme is activated.

Figure 2.6.4 shows the computed water surface along cuts at  $x = 110m$  and  $y = 130m$ . The numerical results from Fennema and Chaudhry [20] and from Biscarini *et al.* [21] and are also depicted for comparison. Fennema used a shallow water model solved with an implicit finite difference method. Biscarini used the 2D shallow water open-source code CCHE2-D and the full 3D Navier-Stokes multiphase equations implemented in OpenFOAM. The global shape of the height is in good agreement with the reference results. The 3D results from Biscarini show a water surface immediately upstream of the gate lower than those predicted by the shallow water codes because of the gravity force implemented in the full Navier-Stokes equations. The 2nd order computation with MUSCL method shows a region of peak/valley in the range  $50 \leq x \leq 100$  whereas the 1st order computation does not show such a region.

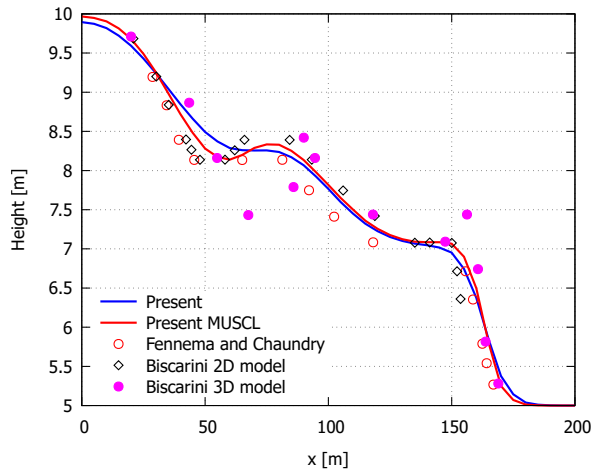
Figure 2.6.5 shows hydrographs at four different monitor points (these points are represented on Fig. 2.6.1). As underlined by Biscarini, the shallow water models tend to underestimate the



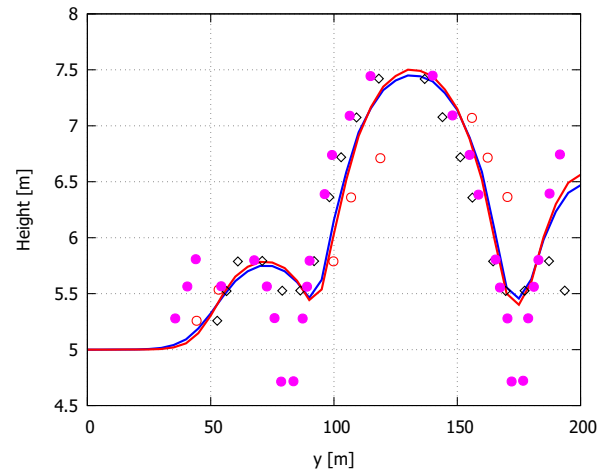
**Figure 2.6.2:** Partial dam breach - Iso-value lines of the water height and velocity arrays at  $t = 7.2s$ .



**Figure 2.6.3:** Partial dam breach - Water surface at  $t = 7.2s$ .



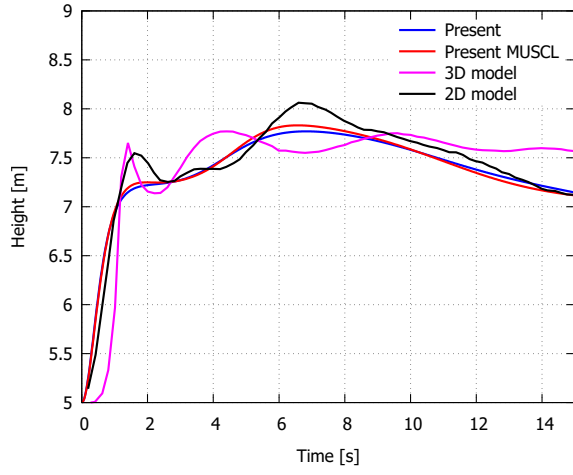
(a) Horizontal cut at  $y = 130m$



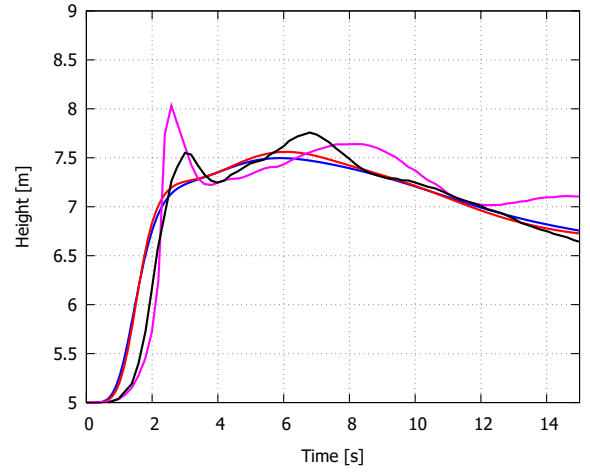
(b) Vertical cut at  $x = 110m$

**Figure 2.6.4:** Partial dam breach - Water elevation 7.2s after the dam break. Comparison with the numerical results from Fennema and Chaudhry [20] and from Biscarini *et al.* [21]

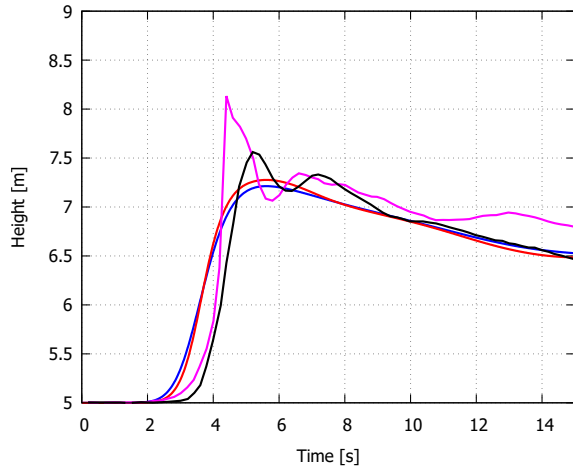
water level and the frontwave celerity.



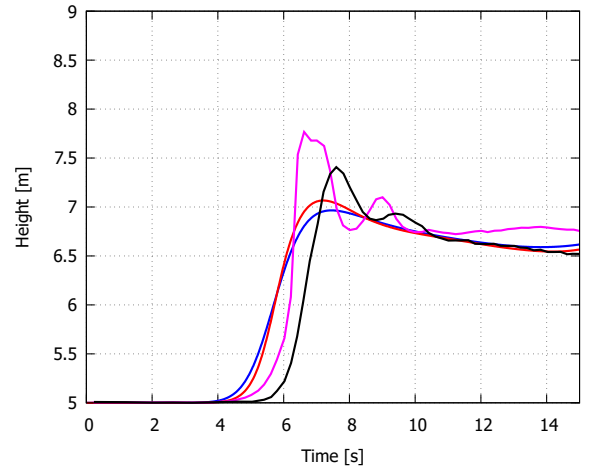
(a) Point at  $(x = 100m, y = 130m)$



(b) Point at  $(x = 110m, y = 130m)$



(c) Point at  $(x = 130m, y = 130m)$



(d) Point at  $(x = 150m, y = 130m)$

**Figure 2.6.5:** Partial dam breach - Water elevation as a function of time at four monitor points. Comparison with the numerical results from Biscarini *et al.* [21]

# Bibliography

- [1] de Saint Venant. Théorie du mouvement non permanent des eaux avec applications aux crues des rivières et à l'introduction des marées dans leur lit. *Comptes Rendus de l'Académie des Sciences de Paris*, 73:148–154, 237–240, 1871.
- [2] V.T. Chow. *Open-Channel Hydraulics*. McGraw-Hill, Inc., New York, N.Y., 1959.
- [3] P. Brufau and P. Garcia-Navarro. Two-dimensional dam break flow simulation. *International Journal for Numerical Methods in Fluids*, 33(1):35–57, 2000.
- [4] B. van Leer. Towards the ultimate conservative difference scheme III. Upstream-centered finite-difference schemes for ideal compressible flow. *Journal of Computational Physics*, 23:263–275, 1977.
- [5] A. Bermúdez, Dervieux A., J.-A. Désidéri, and Vázquez M.E. Upwind schemes for the two-dimensional shallow water equations with variable depth using unstructured meshes. Technical Report 2738, 1995.
- [6] M.J. Castro, J.A. García-Rodríguez, J.M. González-Vida, and C. Parés. A parallel 2d finite volume scheme for solving systems of balance laws with nonconservative products. Application to shallow flows. *Computer Methods in Applied Mechanics and Engineering*, 195:2788–2815, 2006.
- [7] Slah Sahmim. *Un schéma aux volumes finis avec matrices signe pour les systèmes non homogènes*. PhD thesis, Université Paris-Nord, Paris XIII, 2005.
- [8] C.-W. Shu and S. Osher. Efficient implementation of essentially non-oscillatory shock capturing schemes. Technical Report ICASE Report No 87-33, NASA, 1987.
- [9] M.H. Chaudhry. *Open-Channel Flow, Second Edition*. Springer Science+Business Media, LLC, New York, NY, USA, 2008.
- [10] L. Cueto-Felgueroso, D. Santillán, J.H. García-Palacios, and L. Garrote. Comparison between 2D shallow-water simulations and energy-momentum computations for transcritical flow past channel contractions. *Water*, 11(7):1476, 2019.
- [11] T.H.Y. Yoon and S.-K. Kang. Finite volume model for two-dimensional shallow water flows on unstructured grids. *Journal of Hydraulic Engineering*, 130(7), 2004.
- [12] A. Valiani, V. Caleffi, and A. Zanni. Finite volume scheme for 2D shallow-water equations. Application to the Malpasset dam-break. In *Proceedings of the 4th CADAM Meeting*. 18-19 November 1999, Saragozza, Spain, 1999.
- [13] U.S. Army Corps of Engineers. Hydraulic design of flood control channels. Technical Report 1110-2-1601, Department of the Army, Washington D.C. 20314-1000, 1994.

- [14] W. Lai and A.A. Khan. A discontinuous Galerkin method for two-dimensional shock wave modeling. *Modelling and Simulation in Engineering*, Article ID 782832, 2011.
- [15] R.C. Berger and R.L. Stockstill. Finite-element model for high-velocity channels. *Journal of Hydraulic Engineering*, 121(10):710–716, 1995.
- [16] H. Lee. Application of Runge-Kutta discontinuous Galerkin finite element method to shallow water flow. *KSCE Journal of Civil Engineering*, 18(5):1554–1562, 2014.
- [17] A. Ippen and J.H. Dawson. Design of channel contractions. In *High-velocity flow in open channels: a symposium*, volume 116. Transactions of the American Society of Civil Engineers, 1951.
- [18] C. Geuzaine and J.-F. Remacle. Gmsh: a three-dimensional finite element mesh generator with built-in pre- and post-processing facilities. *International Journal for Numerical Methods in Engineering*, 79(11):1309–1331, 2009.
- [19] A. Defina and D.P. Viero. Open channel flow through a linear contraction. *Physics of Fluids*, 22:036602, 2010.
- [20] R.J. Fennema and M.H. Chaudhry. Explicit methods for two-dimensional transient free-surface flows. *Journal of Hydraulic Engineering*, 116(8):1013–1034, 1990.
- [21] C. Biscarini, S. di Francesco, and P. Manciola. CFD modelling approach for dam break flow studies. *Hydrology and Earth System Sciences*, 14:705–718, 2010.